© Copyright by

Burcin Ozcan

December 2015

IMAGE ANALYSIS USING DIRECTIONAL MULTISCALE REPRESENTATIONS AND APPLICATIONS FOR CHARACTERIZATION OF NEURONAL MORPHOLOGY

A Dissertation Presented to

the Faculty of the Department of Mathematics

University of Houston

In Partial Fulfillment

of the Requirements for the Degree

Doctor of Philosophy

By

Burcin Ozcan

December 2015

IMAGE ANALYSIS USING DIRECTIONAL MULTISCALE REPRESENTATIONS AND APPLICATIONS FOR CHARACTERIZATION OF NEURONAL MORPHOLOGY

Burcin Ozcan

Approved:

Dr. Emanuel Papadakis(Committee Chair)
Department of Mathematics, University of Houston

Dr. Demetrio Labate
Department of Mathematics, University of Houston

Dr. Bernhard G. Bodmann
Department of Mathematics, University of Houston

Dr. Fernanda Laezza
Department of Pharmacology and Toxicology, The University of Texas Medical Branch

---

Dean, College of Natural Sciences and Mathematics
University of Houston

Acknowledgements

There are many people that I would like to thank when I look back to my years at University of Houston. This work would not have been possible without their support, collaboration, and guidance. First and foremost, I would like to express my deepest gratitude to my doctoral advisor Professor Manos Papadakis for giving me the opportunity to work with him. I feel very fortunate to have such an interesting and beautiful thesis project. Despite his busy schedule, he was always ready to meet and discuss my progress. His conversations inside and outside the project were invaluable for me.

I am also very thankful to Professor David Jimenez for his sincere effort and taking the time to teach me the project that I participated in. Without his help and never-ending interest in our various ongoing investigations, it wouldn't have been possible to enjoy the project.

I would like to thank Professor Demetrio Labate for his support for our work. I also would like to thank Professor Fernanda Laezza and her lab for their willingness to provide both data and expertise. I want to thank Professor Bernhard G. Bodmann for his useful remarks and feedback for the thesis.

I would also want to thank Paul and Sanat for sharing their computational skills and knowledge.

I would like to thank all the professors and staff members in the Mathematics Department, University of Houston.

Special thanks go to my friends Mauricio, especially, Ricky and Satish for joyful conversations and for always being there for me when I'm down or need help. I will miss our conversations. I also thank Esra, Ali, Arjun, and Nikita for their support during my first

year at University of Houston.

Last but not the least, I would like to mention the great support and faith I have received from my family without which it wouldn't have been possible to reach this goal.

IMAGE ANALYSIS USING DIRECTIONAL MULTISCALE REPRESENTATIONS AND APPLICATIONS FOR CHARACTERIZATION OF NEURONAL MORPHOLOGY

An Abstract of a Dissertation

Presented to

the Faculty of the Department of Mathematics

University of Houston

In Partial Fulfillment

of the Requirements for the Degree

Doctor of Philosophy

By

Burcin Ozcan

December 2015

Abstract

Recent advances in high-resolution fluorescence microscopy have enabled the systematic study of morphological changes in large populations of cells induced by chemical and genetic perturbations, facilitating the discovery of signaling pathways underlying diseases and the development of new pharmacological treatments. In these studies, though, quantification and analysis of morphological features are for the vast majority processed manually, slowing data processing significantly and limiting the information gained to a descriptive level. As an example, automated identification of the primary components of a neuron and extraction of its features are essential steps in many quantitative studies of neuronal networks. Recent advances in applied harmonic analysis, especially in the area of multiscale representations, offer a variety of techniques and ideas which have potential to impact this field of scientific investigation. Motivated by the properties of directional multiscale representations, the focus of this thesis is to introduce a new notion, *directional ratio*, which is a multiscale quantitative measure, capable of distinguishing isotropic from anisotropic structures and the characterization of local isotropy.

Another part of the dissertation illustrates the application of *directional ratio*. In particular, we present an algorithm for automated soma extraction and separation of contiguous somas. Our numerical experiments show that this approach is reliable and efficient to detect and segment somas.

Contents

List of Figures

List of Tables

Chapter 1

Background and Motivation

1.1 Introduction

Foundations of wavelet theory were laid in the 1980's to provide sparse representations for functions with point discontinuities [37]. The concept of sparsity in representations predates wavelets. In the context of wavelets and similar representations, the key to sparsity is that discontinuities and other types of singularities affect the magnitude of the transform locally and not globally. Moreover, smooth regions result in only a few coarse-scale significant non-zero transform coefficients. The basic idea at the core of this approach is to generate a family of waveforms ranging over several scales and locations through the actions of dilation and translation operators on a fixed 'mother' function. Despite their useful properties in one dimension, wavelet transforms in higher dimension spaces have poor directional sensitivity, therefore, they do not provide much information about the *geometry* of the singularities of a function defined on a multidimensional domain. In many applications, edge-type discontinuities are frequently the most significant features and it is desirable not only to identify their locations but also capture their orientations. To over-

come this limitation, a new class of improved multiscale methods emerged, including most notably curvelets and shearlets [5, 31], which combine the advantages of multiscale analysis with the ability to efficiently encode directional information. Thanks to their ability to capture the geometry of data, this new generation of multiscale methods can be particularly useful for the extraction of intrinsic geometric features of images. In particular, we have shown in [40, 33, 41] one can use directional transforms such as shearlet transform to study local directional patterns in images. Despite these results demonstrating the impressive geometric capabilities of these new multiscale transforms, there are still many outstanding theoretical problems that need to be addressed in order to harness the full power of these ideas to the complex data like neuronal images. Such outstanding problems include:

- *Restrictive assumptions on generating functions:* Assumptions on generating functions may be too restrictive or even impossible to satisfy in discrete applications. Is it possible to weaken these assumptions? In particular, is it possible to use compactly supported analyzing functions with small supports in directional transforms?

- *Asymptotic vs non-asymptotic estimates:* All results about detection and separation of singularities are formulated as *asymptotic estimates:* They hold only in the limit when scale tends to zero or to its finest asymptotic limit. This is a serious limitation in numerical applications, where only a finite range of scales is available and asymptotic estimates are clearly impractical. How can we go beyond asymptotics?

Our investigation is motivated by the need to develop a new generation of data analysis tools to handle the complex and massive biomedical imaging data made available by recently emerged technologies. High-content screenings (HCS), for instance, require the identification and extraction of multiple morphological features of neurons, such as soma shape and volume, neurite length, and branching properties [34, 18]. Such complex infor-

mation, usually compiled from multi-channel fluorescence images, necessitates automated processing methods to handle large batches of data and establish a confident statistical basis for a reliable prediction model. With an increase in the use of HCS in basic science settings, automated detection of cell compartments from fluorescent images is an area of very active research. Since, automated identification of the primary components of a neuron and extraction of its sub-cellular features are essential steps in quantitative studies.

The challenges to address go beyond the difficulty of dealing with large amounts of data. Fluorescent images of neurons are typically dominated by complex 3D structures with features of interest varying significantly in scale and shape. Thus, the automated detection of sub-cellular components is very challenging in biomedical imaging where the objects of interest are frequently very complex, have a large variability in size and the images contrast is often highly irregular. Of all sub-cellular components of a neuron, somas are among the most difficult to detect automatically in fluorescence images, due to the lack of robust markers and the uneven distribution of fluorescence signals. Automated soma/cell detection methods in many image analysis packages rely on contrast enhancement and image intensity thresholding which aid the identification of somas by creating binary masks. In neuronal cultures, somas are usually visible with the aid of biological markers, neither of which are soma-selective. They are diffusely distributed in the somato-dendritic compartment and, as a result, masks obtained with these markers consists of both somas and dendrites. Nuclear staining, on the other hand, targets only nuclear DNA and excludes the cytoplasmic region of the soma surrounding the nucleus.

To address these challenging data analysis problems, in this thesis, we discuss the identification of certain anatomical characteristics in images of neuronal networks acquired using laser scanning microscopy. Indeed, we developed innovative analytic and computational tools combining the power of harmonic analysis, multiscale methods, and varia-

tional methods for the automated detection and accurate segmentation of somas from high-resolution confocal images of cultured neurons. As each neuron consists of a blob-like cell body, called the soma, and many elongated components called the neurites (including one axon and multiple dendrites). The first essential imaging task is to distinguish two classes of shapes: a class of rather isotropic shapes associated with the somas and a class of highly anisotropic shapes associated with the neurites. There have been some methods proposed for shape classification problems such as blob detection methods to detect blob-like objects and vesselness methods to provide a vesselness measure for tubular objects [35, 14, 36, 45, 16, 17]. These methods use LOG (Laplacian of Gaussians), DOG (Difference of Gaussians) and the eigenvalues of the Hessian of filter intensities [22]. The common drawback of these methods is the sensitivity to the irregularities of fluoresence distribution in the images. One of groundbreaking ideas introduced in [25] uses geometric moments. Since then, moment techniques have been established to be used as shape descriptors. A remarkable example is Zernike moments [51]. They are rotational invariant and could be made to be translation and scale invariant as well. These mathematical properties of Zernike moments make them excellent features to be used as shape descriptors. The features generated by Zernike moments are used in a classifier to classify the images [24]. Our problem is to segment somas from dendrites and axons (tubular structures) in binary images of neurons. In those images, dendrites, axons, and somas form one or more connected components, but somas are not connected components on their own. Therefore, we don't have a problem just recognizing a shape which corresponds to a soma, but we want to segment somas as connected sub-components of connected components. Let alone, we have to segment colluded somas as well. This makes our problem different than the ones where Zernike moments have been successfully used. Even though our approach is different than Zernike moment techniques, they share the common invariant properties

which make both approaches very useful as shape descriptors. On the other hand, vesselness methods are not suitable for our problem since as we described before our problem has colluded somas and this approach is not applicable for segmentation of colluded somas. We will close this discussion with the use of anisotropic filters in other applications. Anisotropic filters have been studied and used in several application domains. Among them are shearlets [31], curvelets [5], and other parabolic or alpha-molecules for which directional ratio can be defined. In fact, we discuss the shearlet-based directional ratio in the next chapter. In our current work, we study a more general concept of directional ratio based on parabolic molecules. Anisotropic filters have also been used for anisotropic difussion, e.g. [53, 30, 56]. After the Perona and Malik paper [43] which introduced this method, a very long series of papers followed proposing various anisotropic filters and applications of the method. Anisotropic diffusion is a variational method and in that sense it bares some similarities with the level set method we use for soma segmentation. This method smooths connected regions without smearing their boundaries. This is why it is widely used in image denoising applications [19, 53, 57]. In order to distinguish anisotropic objects, such as vessel-like structures, from isotropic ones, e.g disk-like shaped objects, we introduce the notion of *Directional Ratio* which is a precise measure of anisotropy of a structure within a certain scale. One of the most interesting features of Directional Ratio is the ability to enhance the directional sensitivity of the underlying directional transform by comparing the magnitude of the local directional content (i.e. local isotropy and anisotropy properties) of a function over the two orientations where the behavior is most dissimilar. Local isotropy and anisotropy are properties tied to a range of scales. The ideas introduced in this section open a new avenue for the detection of singularities organized in space as boundaries of isotropic or vessel-like structures at a certain range of scales. The advantage of this novel point of view is that it bypasses asymptotic analysis in image models and is the backbone

of our work, 'Quantification of phenotypic characteristics in neuronal images', where our objects of interest include blob-like (somas) and vessel-like structures (neurites) of various sizes.

1.2 Notation and Defintions

It is useful to introduce some notations and definitions.

1. $\chi_A(x) = \begin{cases} 1 \quad if \quad x \in A, \\ 0 \quad if \quad x \notin A \end{cases}$
2. $\hat{f}$ denotes the Fourier transform of f.
3. $f^\vee$ denotes the inverse Fourier transform of f.
4. $\text{sinc}(x) := \frac{\sin(2\pi x)}{\pi x} = \left(\chi_{[-1,1]}\right)^\vee(x) \quad$ with $x \in \mathbb{R}$.
5. $T_x f(y) = f(y - x)$ is the translation operator.
6. $\rho(R)f(x) = f(Rx)$ is the rotation operator, where R is a rotation matrix.
7. $D^j_{A_{\alpha,\beta}} f(x) = |\det A_{\alpha,\beta}|^{j/2} f(A^j_{\alpha,\beta} x)$ is the dilation operator where $A_{\alpha,\beta}$ is an anisotropic expanding matrix such that

$$A_{\alpha,\beta} = \begin{pmatrix} a & 0 \\ 0 & a^\beta \end{pmatrix} \tag{1.1}$$

   $a > 1$ and $0 < \beta < 1$.

9. $B(x, r)$ is the open ball of radius r centered at x in $\mathbb{R}^2$

1.3 The Shearlet Transform

For appropriate admissible functions $\psi^{(h)}, \psi^{(v)} \in L^2(\mathbb{R}^2)$ and matrices

$$M_{as} = \begin{pmatrix} a & -\sqrt{a}s \\ 0 & \sqrt{a} \end{pmatrix}, \quad N_{as} = \begin{pmatrix} \sqrt{a} & 0 \\ -\sqrt{a}s & a \end{pmatrix},$$

we define the *horizontal* and *vertical (continuous) shearlets* by

$$\psi^{(h)}_{a,s,t}(x) = |\det M_{as}|^{-\frac{1}{2}} \psi^{(h)}(M_{as}^{-1}(x-t)), \quad a > 0, s \in \mathbb{R}, t \in \mathbb{R}^2,$$

and

$$\psi^{(v)}_{a,s,t}(x) = |\det N_{as}|^{-\frac{1}{2}} \psi^{(v)}(N_{as}^{-1}(x-t)), \quad a > 0, s \in \mathbb{R}, t \in \mathbb{R}^2,$$

respectively. The reason for choosing two systems of analyzing functions is to ensure a more uniform covering of the range of directions through the shearing variable s. Indeed, rather than using a single shearlet system where s ranges over $\mathbb{R}$, we will use the two systems of shearlets defined above and let s range over a finite interval only.

To define our admissible functions $\psi^{(h)}, \psi^{(v)}$, for $\xi = (\xi_1, \xi_2) \in \mathbb{R}^2$, let

$$\hat{\psi}^{(h)}(\xi_1, \xi_2) = \hat{\psi}_1(\xi_1)\, \hat{\psi}_2(\tfrac{\xi_2}{\xi_1}), \quad \hat{\psi}^{(v)}(\xi_1, \xi_2) = \hat{\psi}_1(\xi_2)\, \hat{\psi}_2(\tfrac{\xi_1}{\xi_2}),$$

where $\hat{\psi}_1$, $\hat{\psi}_2 \in C^\infty(\mathbb{R})$ and satisfy the following conditions:

$$\int_0^\infty |\hat{\psi}_1(a\omega)|^2 \frac{da}{a} = 1, \text{ for a.e. } \omega \in \mathbb{R}, \text{ and } \operatorname{supp}\hat{\psi}_1 \subset [-2, -\tfrac{1}{2}] \cup [\tfrac{1}{2}, 2];$$
$$\|\psi_2\|_2 = 1 \text{ and } \operatorname{supp}\hat{\psi}_2 \subset [-\tfrac{\sqrt{2}}{4}, \tfrac{\sqrt{2}}{4}].$$

Observe that, in the frequency domain, a shearlet $\psi^{(h)}_{a,s,t}$ has the form:

$$\hat{\psi}^{(h)}_{a,s,t}(\xi_1,\xi_2) = a^{\frac{3}{4}}\hat{\psi}_1(a\,\xi_1)\,\hat{\psi}_2(a^{-1/2}(\tfrac{\xi_2}{\xi_1}-s))\,e^{-2\pi i\xi\cdot t}.$$

This shows each function $\hat{\psi}^{(h)}_{a,s,t}$ has the following support:

$$\operatorname{supp}\hat{\psi}^{(h)}_{a,s,t} \subset \{(\xi_1,\xi_2) : \xi_1 \in [-\tfrac{2}{a},-\tfrac{1}{2a}]\cup[\tfrac{1}{2a},\tfrac{2}{a}],\ |\tfrac{\xi_2}{\xi_1}-s| \le \sqrt{a}\}.$$

That is, the frequency support of $\hat{\psi}^{(h)}_{a,s,t}$ is a pair of trapezoids, symmetric with respect to the origin, oriented along a line of slope s.

The horizontal and vertical shearlets form a collection of functions ranging not only over various locations and scales, like the elements of a traditional wavelet system, but also over various orientations controlled by the variable s, and with frequency supports becoming highly anisotropic at fine scales ($a \to 0$). In space domain, these functions are not compactly supported but their supports are essentially concentrated on orientable rectangles with side-lengths a, $\sqrt{a}$ and orientation controlled by s. The support becomes increasingly thin as $a \to 0$. The frequency supports of some representative horizontal shearlets are illustrated in Figure 1.1.

Using the horizontal and vertical shearlets, we define the *(fine-scale) continuous shearlet transform* on $L^2(\mathbb{R}^2)$ ([31]) as the mapping

$$f \in L^2(\mathbb{R}^2 \setminus [-2,2]^2)^\vee \to \mathcal{SH}_\psi f(a,s,t), \quad a \in (0,\tfrac{1}{4}], s \in [-\infty,\infty], t \in \mathbb{R}^2,$$

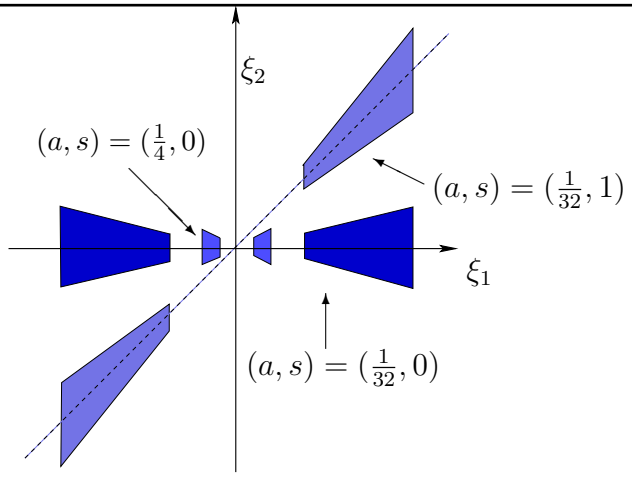

Figure 1.1: Frequency supports of the horizontal shearlets $\hat{\psi}^{(h)}_{a,s,t}$ for different values of a and s.

given by

$$\mathcal{SH}_\psi f(a,s,t) = \begin{cases} \mathcal{SH}^{(h)}_\psi f(a,s,t) = \langle f, \psi^{(h)}_{a,s,t}\rangle, & \text{if } |s| \leq 1 \\ \mathcal{SH}^{(v)}_\psi f(a,\frac{1}{s},t) = \langle f, \psi^{(v)}_{a,\frac{1}{s},t}\rangle, & \text{if } |s| > 1. \end{cases} \tag{1.2}$$

In the above expression, we adopt the convention that the limit value of $\mathcal{SH}_\psi f(a,s,t)$ for $s = \pm\infty$ is set equal to $\mathcal{SH}^{(v)}_\psi f(a,0,t)$.

The term *fine-scale* refers to the fact that the shearlet transform, $\mathcal{SH}_\psi f$, given by (1.2), is only defined for the "fine scales" scale variable $a \in (0, 1/4]$.

The discrete shearlet transform is obtained by sampling (1.2) at $a = 2^{-2j}$, $s = 2^{-j}\ell$, $t = B_{2^{-j}\ell}A_{2^{-2j}}k$, for $j, \ell \in \mathbb{Z}$, $k \in \mathbb{Z}^2$. In this case, with an abuse of notation, we write the *discrete shearlet transform* as the mapping

$$f \to \mathcal{SH}_\psi f(j,\ell,k) = \langle f, \psi_{j,\ell,k}\rangle, \quad j,\ell \in \mathbb{Z}, k \in \mathbb{Z}^2.$$

This transform inherits some useful analytic properties from its continuous counterpart and

can be implemented by fast wavelet-like algorithms.

Chapter 2

Directional Ratio

This chapter presents ideas published in our prior work [40, 33].

2.1 Motivation

One of the main problems in image analysis is the extraction of shape characteristics. Understanding complex shapes can be a very challenging problem especially in the domain of natural images where the variety of shapes can easily be overwhelming. However, our analysis is focused on a certain type of images which by all means are not natural in the usual sense. The class of images of interest are images of clusters of neurons acquired with laser scanning microscopes. Thus, the problem of extraction of shape characteristics is presented in a simpler way because we want to distinguish two classes of shapes: Tubular from non-tubular, or more generally anisotropic shapes from isotropic ones. In images of clusters of neuronal cells where, acquired with laser scanning microscopes, the only objects that are present are dendritic branches, axons, and somas. The former are tubular structures, thus, anisotropic, while the latter express anisotropy to much lesser degree. Needless to

say, any notion of isotropy vs. anisotropy depends on the scale at which the structures of interest are being considered. For instance, a thick tube can be regarded within a relatively small image patch as an isotropic structure, but, if it is seen as a part of a relatively larger patch, its anisotropy becomes evident. In the course of our presentation, another feature akin to the data representation filters, the local aspect ratio, will be emerge as a factor for the robust performance of the anisotropy quantification metric. As a last note, we remark that a second shape characteristic of the imaged structure plays a significant role: the local directionality of the structure, which can be intuitively described as the orientation of its ”principal” axis, if any, of the restriction of the structure within a certain image patch. Again, intuitively speaking, all these features taken together can be used to characterize anisotropy. Although, one can easily understand why scale and local directionality can influence the detection of the presence of anisotropy, this is not necessarily true with local aspect ratio since this is a property of the data representation filters.

Thus, in order to distinguish anisotropic objects, such as tubular-like, structures, from isotropic ones, e.g disk-like shaped objects, we define the notion of Directional Ratio which is a measure of anisotropy of a structure. The presence of this new concept can be defined for every transform or analysis operator induced by families of directional atoms.

2.2 Directional Ratio for Haar-like Functions

We begin by introducing the concept of directional ratio with a class of very simple analyzing functions. We present the development of this novel concept in a way that reflects the timeline of the development of this concept which constitutes the main topic of this thesis. The parameters determining this family clarify how scale, aspect ratio, and orientation affect the values of directional ratio. Although, the following presentation of concepts and

development of the theory is for 2-D, all of it extends verbatim to 3-D. Directional ratio can be computed for any image. However, our theoretical analysis of the behavior of this new concept considers cartoon images which are of the form χ_A, where A is a subset of $\mathbb{R}^2$.

Definition 2.1. Let $A \subset \mathbb{R}^2$. If $x \in A$ we say that x is a *point of local isotropy* of A at scale $s > 0$ if $B(x, s/2) \subseteq A$.

Obviously, the scale at which the isotropy is observed is not unique. For example, let A be a ball of radius $S > 0$. Then, the ball at its center is locally isotropic at any radius up to scale $2S$. This definition attempts to establish a first connection between the geometric property of the radius of a ball and scale. Recall, that scale is a property of the physical domain defined in the Fourier domain in terms of dyadic decompositions introduced by Littlewood and Paley [7]. Intuitively speaking, the spatial extend of an object dictates its "essential support" in the frequency domain which can be thought of as the subset of the frequency domain supporting the main part of the Fourier transform of the characteristic function of this isotropic patch.

As the point of interest moves closer to the boundary, the scale of isotropy is being reduced, as expected. On the antipodal end, suppose that we have a tubular structure and, in particular, a cylinder of radius r then, at any point of its centerline the tubular structure has local isotropy of scale up to $2r$, but that property seizes to be true for scales greater than $2r$. Furthermore, at a relatively small scale and in every structure with non-empty interior, an interior point can be regarded as a point of local isotropy. These observations underpin the relationship with anisotropy and scale. They also help us understand how a traditional topological property, that, of a point being in the interior of a set, in this new framework of local isotropy at a certain scale introduced by Definition 2.1, is in the heart of the apparatus which we are building in order to detect the presence of an anisotropic

or isotropic structure at a certain scale. This apparatus is a simple thresholding operation applied on new function called Directional Ratio. The definition below (Eq. 2.2) is our first attempt to develop this concept and uses a family of Haar-like functions inspired by the Radon transform: Let, $0 < r < s$. Define

$$\chi_{s,r} := \chi_{[-\frac{s}{2},\frac{s}{2}]\times[-\frac{r}{2},\frac{r}{2}]} \tag{2.1}$$

and take the family of all of its rotations $\rho(R)\chi_{s,r}$. In practice, we consider only a finite set of rotations. The next result gives some rise to a quantity we call *Directional Ratio, $\mathcal{D}_{s,r}$, for a real valued function f at scale s and at point x* defined by

$$\mathcal{D}_{s,r}f(x) = \frac{\inf_R\{|\langle f, T_x\rho(R)\chi_{s,r}\rangle| : R \in SO(2)\}}{\sup_R\{|\langle f, T_x\rho(R)\chi_{s,r}\rangle| : R \in SO(2)\}} \quad , \tag{2.2}$$

where $0 < r < s$.

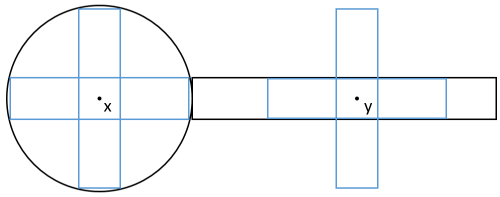

Figure 2.1: Illustration of the main idea of the definition of the function $\mathcal{D}_{s,r}$ given by (2.2). At an appropriate scale by rotating Haar-like functions (in this case the characteristic function of the blue rectangle), we can distinguish whether a point is an interior point of an isotropic object or of an anisotropic object.

Next, we establish the existence of a threshold enabling the detection of the presence of an anisotropy or isotropy in a structure at a certain scale in cartoon-like images which

serve as a simple mathematical model of natural images.

A simple cartoon-like image example is $f = \chi_A$ where A is a subset in $\mathbb{R}^2$. Then the directional ratio for χ_A at scale s and at point x is

$$\mathcal{D}_{s,r}\chi_A(x) = \frac{\inf_R \{|\langle \chi_A, T_x\rho(R)\chi_{s,r}\rangle| : R \in SO(2)\}}{\sup_R \{|\langle \chi_A, T_x\rho(R)\chi_{s,r}\rangle| : R \in SO(2)\}} ,$$

where x is an interior point of A (see Figure 2.2). Note, that when x is an interior point of A the quantity $\mathcal{D}_{s,r}\chi_A(x)$ is well defined for every scale $s > 0$. In any image, since even the finest structures have non-empty interior of width of at least one pixel/voxel, every point in the image is interior to some structure. So the function $\mathcal{D}_{s,r}\chi_A$ can be computed for every pixel/voxel.

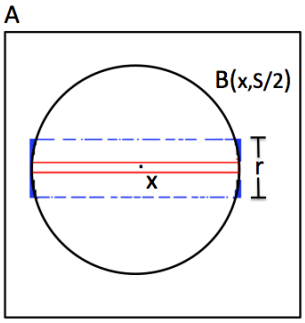

Figure 2.2: Illustration of the main idea of the proof of Proposition 2.2. As $r \to 0$ the parallilepiped $[-\frac{s}{2}, \frac{s}{2}] \times [-\frac{r}{2}, \frac{r}{2}]$ is almost contained in $B(x, s/2)$ if x is a point of isotropy of A at scale s, forcing $\mathcal{D}_{s,r}\chi_A(x) = 1$ as r goes to 0.

Proposition 2.2. *Suppose that A is a compact subset of $\mathbb{R}^2$ and that x is point of local isotropy of A at scale S. Then, $\lim_{r\to 0} \mathcal{D}_{s,r}\chi_A(x) = 1$ for every $0 < s \leq S$. Moreover, $\mathcal{D}_{s,r}\chi_A$ is locally rotationally invariant at scale s and it also obeys a simple covariance rule under the action of rigid motions:*

1) For any rigid motion Q, the directional ratio of $Q(A)$ at Qx at any scale is equal to

directional ratio of A at x at the same scale.

2) *Last, $\mathcal{D}_{s,r}\chi_A$ obeys a simple scale covariance rule: For every closed subset A and scale s, the directional ratio for aA at ax, $\mathcal{D}_{as,r}\chi_{aA}(ax)$ is equal to the directional ratio for A at x $\mathcal{D}_{s,r}\chi_A(x)$*

Proof. If x is a point of local isotropy of A at scale S then the ball $B(x, S/2)$ is contained in A. Then, for a fixed $s \leq S$ and any rotation R we have

$$\lim_{r\to 0} \left\langle \chi_{A\setminus B(x,\, S/2)},\ T_x\rho(R)\chi_{s,r} \right\rangle = 0\ . \tag{2.3}$$

Moreover, the radial symmetry of $B(0, S/2)$ implies that for every $0 < r < s$ we have $\left\langle \chi_{B(x,S/2)},\ T_x\rho(R)\chi_{s,r} \right\rangle = \left\langle \chi_{B(0,S/2)},\ \rho(R)\chi_{s,r} \right\rangle = \left\langle \chi_{B(0,S/2)},\ \chi_{s,r} \right\rangle$. The right-hand side of the previous equation depends only on r. So,

$$\frac{\inf_R\{|\left\langle \chi_A, T_x\rho(R)\chi_{s,r}\right\rangle| : R \in SO(2)\}}{\sup_R\{|\left\langle \chi_A, T_x\rho(R)\chi_{s,r}\right\rangle| : R \in SO(2)\}} =$$

$$\frac{\inf_R\{|\left\langle \chi_{B(0,S/2)}, \rho(R)\chi_{s,r}\right\rangle + \left\langle \chi_{A\setminus B(x,S/2)}, T_x\rho(R)\chi_{s,r}\right\rangle| : R \in SO(2)\}}{\sup_R\{|\left\langle \chi_{B(0,S/2)}, \rho(R)\chi_{s,r}\right\rangle + \left\langle \chi_{A\setminus B(x,S/2)}, T_x\rho(R)\chi_{s,r}\right\rangle| : R \in SO(2)\}}$$

which due to Eq. (2.3) implies

$$\lim_{r\to 0} \frac{\inf_R\{|\left\langle \chi_A, T_x\rho(R)\chi_{s,r}\right\rangle| : R \in SO(d)\}}{\sup_R\{|\left\langle \chi_A, T_x\rho(R)\chi_{s,r}\right\rangle| : R \in SO(d)\}} = 1\ .$$

Now, we turn our attention to the proof of the second statement of Proposition 2.2. By local rotational invariance, we mean an invariance with respect to a rotation centered at x. Such a rotation is the composition, first, of a shift by $-x$ moving the origin to x, then of a

rotation and finally of a shift by x. Thus, the action of a local rotation centered at x on A is expressed by the action of the corresponding operators on χ_A. Therefore, the characteristic function of the set A transformed under the action of the local rotation centered at x is equal to $T_x\rho(Q)T_{-x}\chi_A$, where Q is rotation matrix. Thus, for all s, r we have

$$\langle T_x\rho(Q)T_{-x}\chi_A, T_x\rho(R)\chi_{s,r}\rangle = \langle T_{-x}\chi_A, \rho(Q)^*\rho(R)\chi_{s,r}\rangle = \langle \chi_A,\ T_x(\rho(Q)^*\rho(R))\chi_{s,r}\rangle\ .$$

Since, $Q^T(SO(2)) = SO(2)$, we infer that the directional ratio of A at scale s and of A transformed under the action of the local rotation are equal. In a similar fashion, we derive the rotational covariance rule: For any $Q \in SO(2)$, the directional ratio of $Q(A)$ at Qx at any scale is equal to the directional ratio of A at x at the same scale. The rule follows easily after observing $\rho(Q)T_{Qx} = T_x\rho(Q)$ and

$$\langle \rho(Q)^*\chi_A, T_{Qx}\rho(R)\chi_{s,r}\rangle = \langle \chi_A, T_x(\rho(Q)\rho(R))\chi_{s,r}\rangle\ ,$$

for all $s, r > 0$. The covariance rule for shifts is derived by adopting the previous steps for rotations. Finally, to prove scale covariance first take $a > 0$, a scaling factor. Define a dilation operator $D_af(y) = f(\frac{y}{a})$, $y \in \mathbb{R}^2$. Observe, $D_a^*T_{ax} = T_xD_a^*$. Next, for $r < s$

$$\langle \chi_{aA}, T_{ax}\rho(R)\chi_{as,ar}\rangle = \langle D_a\chi_A, T_{ax}\rho(R)\chi_{as,ar}\rangle = \langle \chi_A, T_x\rho(R)D_a^*\chi_{as,ar}\rangle = \langle \chi_A, T_x\rho(R)\chi_{s,r}\rangle$$

The previous equations imply that for every scale s, the directional ratio for aA at ax, $\mathcal{D}_{as,r}\chi_{aA}(ax)$, is equal to the directional ratio for A at x, $\mathcal{D}_{s,r}\chi_A(x)$, for every A.

□

Next, we discuss if the converse statement of Proposition 2.2 is true. In particular, let

us assume that if x is an interior point of A and the measure of $B(x, S/2) \cap A^c$ is non-zero. If A is the ball $B(x, S/4)$, obviously $\lambda(B(x, S/2) \cap A^c) > 0$, but still, due to the rotational invariance of $B(x, S/4)$ the directional ratio at x and at scale S is still equal to 1, but x is not a point of isotropy for $B(x, S/4)$ at this scale.

Example 2.3. Consider a rectangle A with width $R > 0$ and finite length. Assume that analyzing function is the characteristic function of a rectangle with width $2a$ such that $0 < 2a < R$ and length $2b$ such that $0 < 2b < R$ and $a < b$. Then the directional ratio of boundary points on A is equal to 1 with any scale s up to R. However, boundary points are not a point of isotropy for any scale s. The proof is entirely geometric and it is illustrated in Figure 2.3

This example suggests that directional ratio alone is not sufficient to characterize points of isotropy of closed sets in 2D. However, with a bit of additional information, it is feasible to obtain a partial converse of the first assertion of Proposition 2.2.

Proposition 2.4. *Assume that A is a compact set with non-empty interior and x is an interior point of A. Moreover, assume that there exists $S > 0$ and a rotation R such that $x + R^T([-\frac{S}{2}, \frac{S}{2}] \times [-\frac{r}{2}, \frac{r}{2}]) \subseteq A$ for some $0 < r \leq S$. If $\lim_{r \to 0} \mathcal{D}_{S,r}\chi_A(x) = 1$, then x is a point of isotropy of A at scale S.*

Proof. Let Q be an arbitrary rotation and $0 < p \leq r$, then we observe

$$| \langle \chi_A, T_x \rho(Q) \chi_{S,p} \rangle | = \| \chi_{A \cap (x + Q^T([-\frac{S}{2}, \frac{S}{2}] \times [-\frac{p}{2}, \frac{p}{2}]))} \| \leq Sp \tag{2.4}$$

Hence,

$$\inf_Q \{ | \langle \chi_A, T_x \rho(Q) \chi_{S,p} \rangle | : Q \in SO(2) \} \leq Sp$$

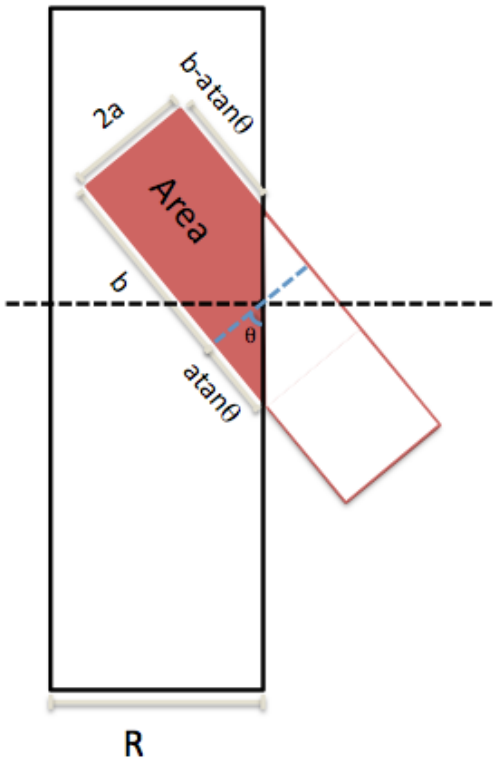

$$\text{Area} = \begin{cases} 2a(b - a\tan\theta + b + a\tan\theta)/2 = 2ab & 0 \leq \theta < \dfrac{\pi}{2} \\ 2ab & \theta = \dfrac{\pi}{2} \end{cases}$$

Figure 2.3: Illustration of the main idea of Example 2.3. As the angle θ (i.e. the direction of the analzing function) changes, the area contained in A doesn't change, forcing $\mathcal{D}_{s,r}\chi_A(x) = 1$ where x is a point on the boundary of A and s is a scale up to R.

On the other hand, the assumption $x + R^T([-\frac{S}{2}, \frac{S}{2}] \times [-\frac{r}{2}, \frac{r}{2}]) \subseteq A$ for some $0 < r \leq S$ and some rotation R implies, due to (2.4),

$$\sup_Q \{ |\langle \chi_A, T_x \rho(Q) \chi_{S,p} \rangle| : Q \in SO(2) \} = Sp \, .$$

To complete the proof, we need to establish $B(x, S/2) \subseteq A$. Assume, that the contrary is true. Let $y \in B(x, S/2) \cap A^c$. Since A is closed, there exists $0 < p_0 < r$ such that $B(y, p_0) \subset B(x, S/2) \cap A^c$. Since $\mathcal{D}_{S,r} \chi_A(x) = 1$ as r goes to 0, for any given $\epsilon > 0$ and every $0 < p < p'$, where $p' < p_0/2$ we have

$$\frac{\inf_Q \{ |\langle \chi_A, T_x \rho(Q) \chi_{S,p} \rangle| : Q \in SO(2) \}}{\sup_Q \{ |\langle \chi_A, T_x \rho(Q) \chi_{S,p} \rangle| : Q \in SO(2) \}} \geq 1 - \epsilon \, .$$

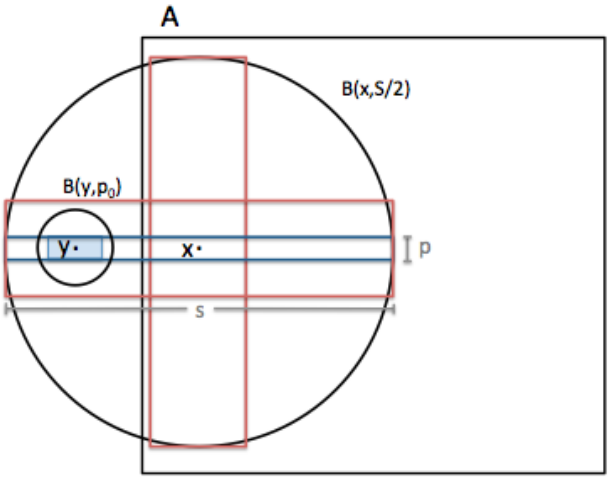

Figure 2.4: Illustration of the main idea of the proof of Proposition 2.4

.

The previous inequality is also valid for an orientation $Q_0 \in SO(2)$ which moves the axis of the slab $x + R^T([-\frac{S}{2}, \frac{S}{2}] \times [-\frac{r}{2}, \frac{r}{2}])$ to the line segment connecting x and y. Then,

inside the ball $B(y, p_0)$ we can find a smaller slab

$$y + Q_0^T \left(\left[-\frac{p_0}{2}, \frac{p_0}{2} \right] \times \left[-\frac{p}{2}, \frac{p}{2} \right] \right) .$$

This slab resides inside the bigger slab $x + Q_0^T([-\frac{S}{2}, \frac{S}{2}] \times [-\frac{p}{2}, \frac{p}{2}])$. However, the smaller slab is not contained in A but it is contained in A^c. Therefore,

$$\frac{Sp - p_0 p}{Sp} \geq \frac{|\langle \chi_A, T_x \rho(Q_0) \chi_{S,p} \rangle|}{Sp} = \frac{\inf_Q \{ |\langle \chi_A, T_x \rho(Q) \chi_{S,p} \rangle| : Q \in SO(2) \}}{\sup_Q \{ |\langle \chi_A, T_x \rho(Q) \chi_{S,p} \rangle| : Q \in SO(2) \}} \geq 1 - \epsilon .$$

Consequently, if we select $\epsilon < p_0/S$, then we arrive at a contradiction. This argument completes the proof of this proposition.

□

Example 2.5. Consider a rectangle A with width $R > 0$ and finite length. Assume that the analyzing function is the characteristic function of a rectangle with width a such that $0 < a < R$ and length b such that $4R < b$ and $a < b$. Then the directional ratio of any point x in A is less than τ such that $\tau << 1$ with any scale s greater than R. The claim is geometrically explained in Figure 2.5.

The next theorem uses more general functions in order to characterize local isotropy. We now introduce a more general concept of directional ratio. The role of scaling is now defined via dilation operators and not as in the previous definition. The assumptions on the function ψ are very general.

$$\mathcal{D}_j f(x) = \frac{\inf_R \{ |\langle f, T_x \rho(R) D_M^j \psi \rangle| : R \in SO(2) \}}{\sup_R \{ |\langle f, T_x \rho(R) D_M^j \psi \rangle| : R \in SO(2) \}}$$

where $T_x f(y) = f(y - x)$ is translation operator, $\rho(R) f(x) = f(Rx)$ is rotation operator

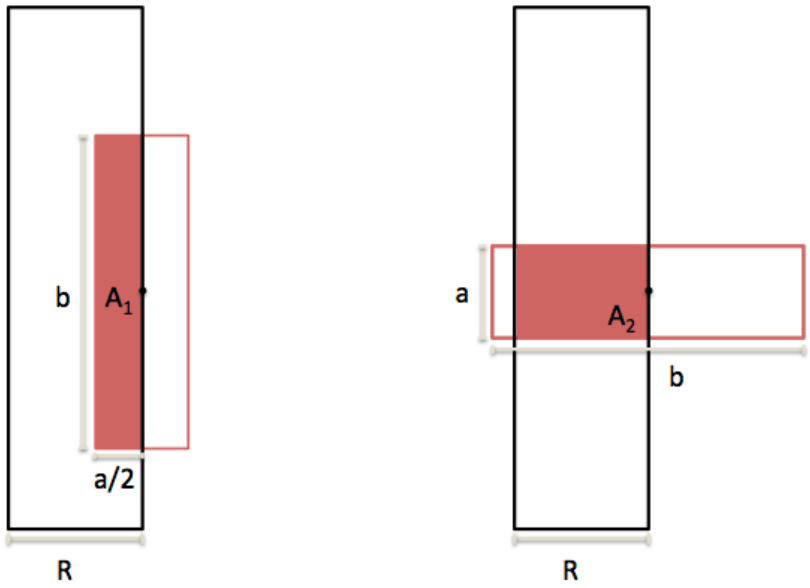

$$A_1 = \frac{b.a}{2} > \frac{4Ra}{2} = 2Ra \qquad A_2 = aR$$

$$\text{Directional Ratio} < \frac{A_2}{A_1} < \frac{aR}{2aR} = \frac{1}{2} << 1$$

Figure 2.5: Illustration of the main idea of the example 2.5. As the angle θ (i.e. the direction of the analzing function) changes, the area contained in A changes significantly, forcing $\mathcal{D}_{s,r}\chi_A(x) << 1$ where x is a point of A and s is a scale greater than R.

and $D_M^j f(x) = |\det M|^{j/2} f(M^j x)$ where M is anisotropic expanding matrix such that

$$M = \begin{pmatrix} a & 0 \\ 0 & a^\beta \end{pmatrix}$$

and $a > 1$, $0 < \beta < 1$.

Theorem 2.6. *Let S be a compact set with nonempty interior and ψ be a measurable function such that $|\psi(x)| \leq \dfrac{C}{(1+\|x\|)^N}$ where $N \geq 1+\delta$, $\delta > 0$ and $\int_{\mathbb{R}^2} \psi(x)dx = 1$. If x_o is a point of local isotropy and $\epsilon > 0$, then there exists a scale $j > 0$ such that $\mathcal{D}_j \chi_S(x_o) > 1 - \epsilon$.*

An example of such a function which satisfies the requirements of the previous theorem is the Haar-like function, defined as (2.1)

Proof. Let us set for convenience $D_M^j \psi(x) = \omega(x)$. We start with the following observation:

$$\begin{aligned} |\langle \chi_S, T_{x_o} \rho(R) D_M^j \psi \rangle| &= |\langle T_{x_o}^* \chi_S, \rho(R)\omega \rangle| = |\langle T_{-x_o} \chi_S, \rho(R)\omega \rangle| \\ &= \left| \int_{\mathbb{R}^2} \chi_S(x + x_o)\omega(Rx)dx \right| \end{aligned}$$

We set $y = Rx$, then we observe :

$$\left| \int_{\mathbb{R}^2} \chi_S(x + x_o)\omega(Rx)dx \right| = \frac{1}{|\det(R)|} \left| \int_{\mathbb{R}^2} \chi_S(R^\top y + x_o)\omega(y)dy \right|$$

Since $\rho : SO(n) \to B(L^2(R^n))$ is continuous and $SO(n)$ is compact, there exist

rotations R_m and R_M such that

$$\min_R\{|\langle \chi_S, T_{x_o}\rho(R)\omega\rangle| : R \in SO(n)\} = |\langle \chi_S, T_{x_o}\rho(R_m)\omega\rangle|$$

and

$$\max_R\{|\langle \chi_S, T_{x_o}\rho(R)\omega\rangle| : R \in SO(n)\} = |\langle \chi_S, T_{x_o}\rho(R_M)\omega\rangle|$$

Note that if $\min$ exists then $\inf$ exists and it is equal to $\min$. Same arguments holds true for $\max$ and it is equal to $\sup$. So,

$$\mathcal{D}_j\chi_S(x_o) = \frac{|\langle|\chi_S, T_{x_o}\rho(R_m)\omega\rangle|}{|\langle \chi_S, T_{x_o}\rho(R_M)\omega\rangle|} = \frac{\frac{1}{|\det(R_m)|}\left|\int_{\mathbb{R}^2}\chi_S(R_m^\top y + x_o)\omega(y)dy\right|}{\frac{1}{|\det(R_M)|}\left|\int_{\mathbb{R}^2}\chi_S(R_M^\top y + x_o)\omega(y)dy\right|}$$

Since in $SO(2)$ the determinant is equal to 1, we have

$$\mathcal{D}_j\chi_S(x_o) = \frac{\left|\int_{\mathbb{R}^2}\chi_S(R_m^\top y + x_o)\omega(y)dy\right|}{\left|\int_{\mathbb{R}^2}\chi_S(R_M^\top y + x_o)\omega(y)dy\right|}$$

We start investigating the numerator. Since x_o is a point of local isotropy, there exists a ball $B = x_o + B(0, r_o) \subset S$.

$$\left|\int_{\mathbb{R}^2}\chi_S(R_m^\top y + x_o)\omega(y)dy\right| = \left|\int_{\mathbb{R}^2}(\chi_B(R_m^\top y + x_o) + \chi_{B^c\cap S}(R_m^\top y + x_o))\omega(y)dy\right|$$

Now we estimate the two integrals resulting from the right-hand side of the previous equation.

$$\left|\int_{\mathbb{R}^2}\chi_B(R_m^\top y + x_o)\omega(y)dy\right| \quad = \quad \left|\int_{\|y\|\le r_o}|\det M|^{j/2}\psi(M^j y)dy\right|$$

$$= |\det M|^{j/2}\left|\int_{\|y\|\le r_o}\psi(M^j y)dy\right|$$

For the second summand the estimate is

$$\begin{aligned}\left|\int_{\mathbb{R}^2}\chi_{B^c\cap S}(R_m^\top y+x_o)\omega(y)dy\right| &= \left|\int_{B(0,r_o)^c\cap R_m(-x_o+S)}|\det M|^{j/2}\psi(M^j y)dy\right| \\ &\le |\det M|^{j/2}\int_{\|y\|\ge r_o}|\psi(M^j y)|dy\end{aligned}$$

Let $\lambda = a^{1/2}$ which is the minimum of the diagonal entries of the matrix M and set $v = M^j y$ then we observe:

$$|\det M|^{j/2}\int_{\|y\|\ge r_o}|\psi(M^j y)|dy \le |\det M|^{-j/2}\int_{\|v\|>\lambda^j}|\psi(v)|dv$$

with the assumption made on ψ, we see that

$$|\det M|^{-j/2}\int_{\|v\|>\lambda^j}|\psi(v)|dv \le |\det M|^{-j/2}\int_{\|v\|>\lambda^j}\frac{C}{(1+\|v\|)^N}dv$$

and

$$\begin{aligned}|\det M|^{-j/2}\int_{\|v\|>\lambda^j}\frac{C}{(1+\|v\|)^N}dv &= |\det M|^{-j/2}\int_{\lambda^j}^{\infty}\frac{C}{(1+r)^N}dr \\ &= \frac{|\det M|^{-j/2}C(\lambda+1)^{1-N}}{N-1}\end{aligned}$$

Similarly, we estimate the denominator. All arguments are the same for the denominator since ball is rotation invariant.

Note that,

$$\mathcal{D}_j\chi_S(x_o) = \frac{\left|\int_{\mathbb{R}^2}(\chi_B(R_m^\top y + x_o) + \chi_{B^c\cap S}(R_m^\top y + x_o))\omega(y)dy\right|}{\left|\int_{\mathbb{R}^2}(\chi_B(R_M^\top y + x_o) + \chi_{B^c\cap S}(R_M^\top y + x_o))\omega(y)dy\right|}$$

Therefore,

$$\begin{aligned}
\mathcal{D}_j\chi_S(x_o) &\geq \frac{|\det M|^{j/2}\left|\int_{\|y\|\leq r_o}\psi(M^j y)dy\right| - \dfrac{|\det M|^{-j/2}C(\lambda+1)^{1-N}}{N-1}}{|\det M|^{j/2}\left|\int_{\|y\|\leq r_o}\psi(M^j y)dy\right| + \dfrac{|\det M|^{-j/2}C(\lambda+1)^{1-N}}{N-1}} \\
&= \frac{|\det M|^{j/2}\left(\left|\int_{\|y\|\leq r_o}\psi(M^j y)dy\right| - \dfrac{C(\lambda+1)^{1-N}}{(N-1)|\det M|^j}\right)}{|\det M|^{j/2}\left(\left|\int_{\|y\|\leq r_o}\psi(M^j y)dy\right| + \dfrac{C(\lambda+1)^{1-N}}{(N-1)|\det M|^j}\right)}
\end{aligned}$$

If we select the scale j sufficiently large so that $\int_{\|y\|\leq r_o}\psi(M^j y)dy > \dfrac{3}{4}$ and $\dfrac{C(\lambda+1)^{1-N}}{(N-1)|\det M|^j} \leq \dfrac{\epsilon}{4}$ then we obtain

$$\mathcal{D}_j\chi_S(x_o) > \frac{3-\epsilon}{3+\epsilon} \geq 1-\epsilon$$

□

Note that the assumption, $\int_{\mathbb{R}^n}\psi(x)dx = 1$, plays a key role in the above proof. Since in order to estimate a lower bound for the directional ratio, we select the scale, j, sufficiently big so that $\int_{\|y\|\leq r_o}\psi(M^j y)dy > \dfrac{3}{4}$ because as $j\to\infty$, $\int_{\|y\|\leq r_o}\psi(M^j y)dy \to 1$. Otherwise, we may end up dividing small numbers which may render the lower estimate of $\mathcal{D}_j\chi_S(x_o)$ uncontrollable.

2.3 Directional Ratio for Shearlets

The concept of *directional ratio* can be defined by means of the continuous shearlet transform. Now, the role of rotations is replaced by shearings. Also, the scale is now implicitly defined via the Fourier transform and not directly as in the previous section. The discussion of the shearlet-based directional ratio is confined in 2-D, although, we believe that it can be extended to 3-D with the appropriate modifications.

The shearlet-based *Directional Ratio* of f at scale $a > 0$ and location $t \in \mathbb{R}^2$ is given by

$$\mathcal{D}_a f(t) = \frac{\inf_s\{|\mathcal{SH}_\psi f(a,s,t)|\}}{\sup_s\{|\mathcal{SH}_\psi f(a,s,t)|\}} \quad , f \in L^2(\mathbb{R}^2), \tag{2.5}$$

and measures the strength of directional information at scale a and location t. The next theorem predicts consistent responses of directional ratio on the anisotropic part of a cartoon neuron S which we define in the statement of the next result.

Theorem 2.7. *Let S be a cylinder with radius $r > 0$ and finite length in the direction of the positive y-half axis. Moreover, assume that ψ is a shearlet defined by ψ_1 and ψ_2 satisfying the following properties :*

1. *the Fourier transforms of both ψ_1 and ψ_2 are C^∞ and even;*
2. *the wavelet function ψ_1 has two "plateaus" in the frequency domain: $\hat{\psi}_1(\xi) = 1$ for all $3/4 \leq |\xi| \leq 3/2$;*
3. *the "bump" function ψ_2 satisfies $\hat{\psi}_2(\xi) = c > 0$ for all $|\xi| \leq 1/4$ and $\int_{-R}^{R} \psi_2(x)dx > 1$ with $R > r > 0$.*

Then, for $4r \leq a \leq 1/4$, there exists a threshold $\tau < 1/3$ such that the shearlet-based

Directional Ratio of χ_S, given by (2.5)*, satisfies:*

$$\mathcal{D}_a\chi_S(y) \leq \tau \qquad y = (y_1, y_2) \quad \textit{sufficiently inside } S. \tag{2.6}$$

With no loss of generality, we can shift the cylinder so that its vertical axis coincides with the y-axis. By "$y = (y_1, y_2)$ being sufficiently inside S" we mean that the rectangle $C = [-r, r] \times [y_2 - R, y_2 + R] \subset S$. We also remark that the constant, c, above must exceed 1 because the support of $\hat{\psi}_2$ is the interval $[-\frac{\sqrt{2}}{4}, \frac{\sqrt{2}}{4}]$ and $||\psi_2||_2 = 1$. Also, with no loss of generality, we can assume that $\hat{\psi}_2(0) = 1$.

Proof. We begin by making clear that the sinc-function is given by

$$\text{sinc}(x) := \frac{\sin(2\pi x)}{\pi x} = \left(\chi_{[-1,1]}\right)^{\vee}(x) \quad \text{ with } x \in \mathbb{R}.$$

With no loss of generality we can shift the origin in order to have $y_2 = 0$. Now, we have:

$$\begin{aligned} \mathcal{D}_a f(y) &= \frac{\inf_s\{|\mathcal{SH}_\psi f(a, s, y)|\}}{\sup_s\{|\mathcal{SH}_\psi f(a, s, y)|\}} \\ &\leq \frac{|\mathcal{SH}_\psi f(a, \infty, y)|}{|\mathcal{SH}_\psi f(a, 0, y)|} \\ &= \frac{|\mathcal{SH}_\psi f^{(v)}(a, 0, y)|}{|\mathcal{SH}_\psi f^{(h)}(a, 0, y)|} \\ &= \frac{|\langle f, \psi^{(v)}_{a,0,y}\rangle|}{|\langle f, \psi^{(h)}_{a,0,y}\rangle|}. \end{aligned} \tag{2.7}$$

The absolute integrability of shearlets implies that, for any $\epsilon > 0$, there exists a square with side of length $2R_0$, such that

$$\int_{([-R_0,R_0]\times[-R_0,R_0])^c} |\psi^{(v)}_{1,0,0}(x, y)|dxdy < \epsilon.$$

and

$$\int_{([-R_0,R_0]\times[-R_0,R_0])^c} |\psi^{(h)}_{1,0,0}(x,y)|dxdy < \epsilon.$$

For technical reasons, we will assume $R_0 > 1/2$. Later in the proof, we will determine ϵ. The above inequality implies that, for both the vertical and horizontal shearlets, we have

$$\int_{([-a^{1/2}R_0,a^{1/2}R_0]\times[-aR_0,aR_0])^c} |\psi^{(v)}_{a,0,0}(x,y)|dxdy < a^{3/4}\epsilon, \tag{2.8}$$

and

$$\int_{([-aR_0,aR_0]\times[-a^{1/2}R_0,a^{1/2}R_0])^c} |\psi^{(h)}_{a,0,0}(x,y)|dxdy < a^{3/4}\epsilon.$$

Our strategy is to show that the numerator in the fraction (2.7) is significantly smaller than the denominator. We begin by estimating the latter.

We stress that we have not specified the quantity ϵ yet, thus, R_0 still needs to be determined. However, we postpone this task until the end of the analysis of the behavior of directional ratio on the tubular part of the cartoon-like neuron.

We will also add the assumption, $R > R_0$. Of course, this additional hypothesis should technically be part of the explanation of the statement "y is sufficiently inside S", but any earlier reference to it would have been hard to appreciate. Note that $\int_{\mathbb{R}} \psi_2(x)dx = 1$ and ψ_2 takes positive and negative values and oscillates to infinity. Therefore, regardless how big R_0 is, we can find $R > R_0$ to satisfy assumption 3 of Theorem 2.7. Our assumptions on R_0 and on the scale a imply $aR_0 \geq 2r$. Consequently, both rectangles $-y + [-r, r] \times [-R, R]$ and $[-aR_0, aR_0]\times[-a^{1/2}R_0, a^{1/2}R_0]$ are contained in the rectangle $[-aR_0, aR_0]\times[-R, R]$.

We observe that

$$\langle f, \psi^{(h)}_{a,0,y}\rangle = \langle T_{-y}f, \chi_{[-aR_0,aR_0]\times[-R,R]}\psi^{(h)}_{a,0,0}\rangle + \langle T_{-y}f, \chi_{([-aR_0,aR_0]\times[-R,R])^c}\psi^{(h)}_{a,0,0}\rangle,$$

which, if combined with $aR_0 \geq 2r$, allows us to take $y_1 = 0$ and to conclude that

$$|\langle f, \psi^{(h)}_{a,0,y}\rangle| > |\langle f\chi_{[-aR_0,aR_0]\times[-R,R]}, \psi^{(h)}_{a,0,0}\rangle| - a^{3/4}\epsilon.$$

Note that χ_S multiplied with $\chi_{[-aR_0,aR_0]\times[-R,R]}$ is equal to $\chi_{[-r,r]\times[-R,R]}$ Thus,

$$|\langle f, \psi^{(h)}_{a,0,y}\rangle| > |\langle \chi_{[-r,r]\times[-R,R]}, \psi^{(h)}_{a,0,0}\rangle| - a^{3/4}\epsilon.$$

We also observe that

$$\begin{aligned}
&|\langle \chi_{[-r,r]\times[-R,R]}, \psi^{(h)}_{a,0,0}\rangle| \\
&= \left| \int_{\frac{1}{2a}<|\xi_1|<\frac{2}{a}} \int_{|\frac{\xi_2}{\xi_1}|<\frac{\sqrt{2a}}{4}} a^{3/4} rR\text{sinc}(r\xi_1)\text{sinc}(R\xi_2)\hat{\psi_1}(a\xi_1)\hat{\psi_2}\left(\frac{\xi_2}{\sqrt{a}\xi_1}\right) d\xi_2\, d\xi_1 \right| \\
&= 2a^{3/4} \left| \int_{\frac{1}{2a}<\xi_1<\frac{2}{a}} r\text{sinc}(r\xi_1)\hat{\psi_1}(a\xi_1) \left(\int_{\frac{|\xi_2|}{\xi_1}<\frac{\sqrt{2a}}{4}} R\text{sinc}(R\xi_2)\hat{\psi_2}\left(\frac{\xi_2}{\sqrt{a}\xi_1}\right) d\xi_2 \right) d\xi_1 \right|,
\end{aligned}$$

where we drop the absolute value of ξ_1 due to the symmetry of the integrand with respect to the ξ_2-axis. First, we estimate the inner integral. To do so, we set $\eta = \frac{\xi_2}{\sqrt{a}\xi_1}$. Then we observe:

$$\int_{\frac{|\xi_2|}{\xi_1}<\frac{\sqrt{2a}}{4}} R\ \text{sinc}(R\xi_2)\hat{\psi_2}\left(\frac{\xi_2}{\sqrt{a}\xi_1}\right) d\xi_2 = \int_{|\eta|<\frac{\sqrt{2}}{4}} \sqrt{a}\xi_1 R\ \text{sinc}(R\sqrt{a}\xi_1\eta)\hat{\psi_2}(\eta) d\eta.$$

Note that

$$\chi_{[-R\sqrt{a}\xi_1, R\sqrt{a}\xi_1]} * \psi_2(0) = \int_{-R\sqrt{a}\xi_1}^{R\sqrt{a}\xi_1} \psi_2(x) dx.$$

Since $c = \hat{\psi_2}(0) = \int_{-\infty}^{\infty} \psi_2(x) dx$, the scale a does not exceed $\frac{1}{4}$, and $\frac{1}{2a} < \xi_1$, and

$\int_{-R}^{R} \psi_2(x)dx > 1$ we conclude $\int_{-R\sqrt{a}\xi_1}^{R\sqrt{a}\xi_1} \psi_2(x)dx > 1$. In conclusion,

$$\int_{\frac{|\xi_2|}{\xi_1} < \frac{\sqrt{2a}}{4}} R\text{sinc}(R\xi_2)\hat{\psi}_2\left(\frac{\xi_2}{\sqrt{a}\xi_1}\right)d\xi_2 > 1. \tag{2.9}$$

Next, we examine the outer integral

$$\int_{\frac{1}{2a}}^{\frac{2}{a}} r\text{sinc}(r\xi_1)\hat{\psi}_1(a\xi_1)d\xi_1 = \int_{\frac{1}{2}}^{2} \frac{r}{a}\text{sinc}\left(\frac{r}{a}\xi\right)\hat{\psi}_1(\xi)d\xi\ .$$

The selection of the scale a implies $0 \leq \frac{r}{a}\xi_1 \leq \frac{1}{2}$ for every value of ξ_1 in the interval of integration. Since the sinc function takes positive values in the open interval $(\frac{1}{2}, 2)$ and $\hat{\psi}_1(\xi) = 1$ for all $\xi \in [\frac{3}{4}, \frac{3}{2}]$, using (2.9), we finally conclude that

$$|\langle f, \psi^{(h)}_{a,0,y}\rangle| > 2a^{3/4}\frac{3}{4}\frac{\sin(\frac{3r\pi}{a})}{\frac{3r\pi}{2a}} - a^{3/4}\epsilon \geq 2a^{3/4}\frac{3}{4}\frac{\sin(\frac{3\pi}{4})}{\frac{3\pi}{8}} - a^{3/4}\epsilon = a^{3/4}\frac{2\sqrt{2}}{\pi} - a^{3/4}\epsilon. \tag{2.10}$$

Now, we turn our attention to the numerator of (2.7); we need to show that it is relatively much smaller than the denominator. We have that

$$\begin{aligned}\langle f, \psi^{(v)}_{a,0,y}\rangle &= \langle T_{-y}f, \chi_{\mathbb{R}\times[-R,R]}\psi^{(v)}_{a,0,0}\rangle + \langle T_{-y}f, \chi_{(\mathbb{R}\times[-R,R])^c}\psi^{(v)}_{a,0,0}\rangle \\ &= \langle T_{-y}(f\chi_{\mathbb{R}\times[-R,R]}), \psi^{(v)}_{a,0,0}\rangle + \langle T_{-y}(f\chi_{(\mathbb{R}\times[-R,R])^c}), \psi^{(v)}_{a,0,0}\rangle\end{aligned}$$

Regardless of how y_1 varies between $-r$ and r, the rectangle $[-\sqrt{a}R_0, \sqrt{a}R_0]\times[-aR_0, aR_0]$ always stays inside the strip $\mathbb{R}\times[-R, R]$, so $|\langle T_{-y}(f\chi_{(\mathbb{R}\times[-R,R])^c}), \psi^{(v)}_{a,0,0}\rangle| \leq a^{3/4}\epsilon$. We also observe that χ_S multiplied with $\chi_{\mathbb{R}\times[-R,R]}$ is equal to $\chi_{[-r,r]\times[-R,R]}$ Therefore, we have that

$$|\langle f, \psi^{(v)}_{a,0,y}\rangle| \leq |\langle T_{-y}\chi_{[-r,r]\times[-R,R]}, \psi^{(v)}_{a,0,0}\rangle| + a^{3/4}\epsilon. \tag{2.11}$$

Note that

$$\langle T_{-y}\chi_{[-r,r]\times[-R,R]}, \psi^{(v)}_{a,0,0}\rangle = \\ a^{3/4}\int_{\frac{1}{2a}<|\xi_2|<\frac{2}{a}}\int_{|\frac{\xi_1}{\xi_2}|<\frac{\sqrt{2a}}{4}} Rr\text{sinc}(r\xi_1)\text{sinc}(R\xi_2)e^{2\pi i\xi_1 y_1}\hat{\psi}_1(a\xi_2)\hat{\psi}_2\left(\frac{\xi_1}{\sqrt{a}\xi_2}\right)d\xi_1\, d\xi_2.$$

Since $\hat{\psi}_2$ is even, we obtain that the latter double integral is equal to

$$a^{3/4}\int_{\frac{1}{2a}<|\xi_2|<\frac{2}{a}}\int_{\frac{-\sqrt{2a}|\xi_2|}{4}}^{\frac{\sqrt{2a}|\xi_2|}{4}} \hat{\psi}_1(a\xi_2)R\text{sinc}(R\xi_2)e^{2\pi i\xi_1 y_1}r\text{sinc}(r\xi_1)\hat{\psi}_2\left(\frac{\xi_1}{\sqrt{a}|\xi_2|}\right)d\xi_1 d\xi_2. \tag{2.12}$$

We now estimate the inner integral. First, using the change of the variable $\eta = \frac{\xi_1}{\sqrt{a}|\xi_2|}$, we obtain that the inner integral in (2.12) is equal to

$$\begin{aligned}\int_{\frac{-\sqrt{2}}{4}}^{\frac{\sqrt{2}}{4}} e^{2\pi i\eta\sqrt{a}|\xi_2|y_1}r\sqrt{a}|\xi_2|\text{sinc}(r\sqrt{a}|\xi_2|\eta)\hat{\psi}_2(\eta)\,d\eta &= \chi_{[-r\sqrt{a}|\xi_2|,r\sqrt{a}|\xi_2|]} * \psi_2(\sqrt{a}|\xi_2|y_1) \\ &= \int_{\sqrt{a}|\xi_2|y_1-r\sqrt{a}|\xi_2|}^{\sqrt{a}|\xi_2|y_1+r\sqrt{a}|\xi_2|}\psi_2(x)dx.\end{aligned}$$

By applying the Cauchy-Schwartz inequality to ψ_2, which has L^2 norm equal to 1, we deduce $||\psi_2||_\infty \leq ||\hat{\psi}_2||_1 < 1$. Therefore, the inner integral in (2.12) is bounded above $2r\sqrt{a}|\xi_2|$. Thus, the absolute value of the integral in (2.12) is bounded above by

$$\begin{aligned}a^{3/4}\int_{\frac{1}{2a}<|\xi_2|<\frac{2}{a}} R|\text{sinc}(R\xi_2)\hat{\psi}_1(a\xi_2)|2r\sqrt{a}|\xi_2|d\xi_2 &= 2a^{3/4}\int_{\frac{1}{2a}}^{\frac{2}{a}} R\frac{|\sin(2\pi R\xi_2)|}{\pi R\xi_2}2r\sqrt{a}\xi_2 d\xi_2 \\ &\leq \frac{12ra^{3/4}}{2\pi\sqrt{a}} \leq \frac{3\sqrt{a}a^{3/4}}{2\pi},\end{aligned}$$

where the last inequality follows from our assumption on the scale a. Using (2.11) and the

last inequality, we obtain that

$$|\langle f, \psi^{(v)}_{a,0,y}\rangle| \leq \frac{3\sqrt{a}a^{3/4}}{2\pi} + a^{3/4}\epsilon.$$

Next, using (2.10), we derive the following upper bound for $\mathcal{D}_a f(y)$:

$$\mathcal{D}_a f(y) \leq \frac{\frac{3\sqrt{a}}{2\pi} + \epsilon}{\frac{2\sqrt{2}}{\pi} - \epsilon}.$$

Taking $\epsilon = \frac{1}{10\pi}$, we get that $\mathcal{D}_a f(y) < \tau := \frac{15\sqrt{a}+1}{20\sqrt{2}-1} < 1/3$, for all $y \in B$.

□

Remark 2.8. *Now, we turn our attention to the set of points of local isotropy. Let us consider the ball A, centered at the origin. We will show that the behavior of the shearlet transform in isotropic regions is not the same as in tubular regions. Morover, if $\epsilon > 0$ is an arbitrary positive number, then, for every $y \in \kappa_\epsilon A$, orientation s and sufficiently fine scale a, where $0 < \kappa_\epsilon < 1$, we have $|\mathcal{SH}_\psi \chi_A(a, s, y)| < \epsilon$.*

Since the ball A is centered at the origin, it is enough to prove the statement for horizontal shearlets only. As we did in the first part of the above proof, for each arbitrary $\epsilon > 0$, we can find a square with side of length $2R_{0,\epsilon}$ such that

$$\int_{([-R_{0,\epsilon},R_{0,\epsilon}]\times[-R_{0,\epsilon},R_{0,\epsilon}])^c} |\psi^{(h)}_{1,0,0}(x, y)|dxdy < \epsilon.$$

The shearing parameter s varies between -1 and 1 and, as it does so, it "shears" the square $Q := [-R_{0,\epsilon}, R_{0,\epsilon}] \times [-R_{0,\epsilon}, R_{0,\epsilon}]$. Therefore, if the scale is sufficiently fine, it is not

hard to see that there exists $0 < \kappa_\epsilon < 1$ *such that*

$$y + M_{as}(Q) \subset A,$$

for every $y \in \kappa_\epsilon A$. *Now, let* $-1 \leq s \leq 1$. *Then* $|\mathcal{SH}_\psi \chi_A(a,s,y)| = |\langle \chi_A, \psi^{(h)}_{a,s,y} \rangle|$. *However,* $\int_{\mathbb{R}} \int_{\mathbb{R}} \psi^{(h)}_{a,s,y} = 0$. *Thus,*

$$\langle \chi_A, \psi^{(h)}_{a,s,y} \rangle = \int_{\mathbb{R}^2} (\chi_A - 1)\overline{\psi^{(h)}_{a,s,y}} = \int_{(y+M_{as}(Q))^c} (\chi_A - 1)\overline{\psi^{(h)}_{a,s,y}},$$

because $y + M_{as}(Q) \subseteq A$. *Therefore, we conclude that*

$$|\mathcal{SH}_\psi \chi_A(a,s,y)| < \int_{(y+M_{as}(C))^c} |\chi_A - 1||\psi^{(h)}_{a,s,y}| < 2a^{3/4}\epsilon < \epsilon.$$

This remark illustrates the behavior of the shearlet transform in isotropic regions. We don't have to take the ϵ very small because, as the scale becomes finer and finer, the quantity $2a^{3/4}\epsilon$ decreases as well. In any case, the main implication of the previous observation is that the shearlet transform will attain very small values everywhere in the isotropic part of the cartoon-like neuron, as long as the location variable of the transform is away from the boundaries. As a result, the values of the Directional Ratio $\mathcal{D}_a \chi_A$ will vary wildly in isotropic regions and, consequently, the Directional Ratio is not useful to detect such regions.

Remark 2.9. *Our observation show that, if* $f = \chi_S$ *and* y *is located inside the rectangular region then, for some suitable scale* $a > 4r$, *there exists a fixed* τ *such that* $\mathcal{D}_a f(y) < \tau$ *and the threshold* τ *does not depend on* y *(Theorem 2.7). This behavior, which is no longer true when* y *is inside the ball of radius* R, *follows from the fact that there are two orientations*

at y, one parallel to the axis of the rectangle and the other perpendicular to it, such that the magnitude of the shearlet transform attains a relatively big value for the former and a small value for the latter. This observation is consistent with the asymptotic behavior of the shearlet transforms as $a \to 0$. However, the remarkable new concept in this result is that the scale a does not need to be very small, but it has to be comparable with the width of the rectangular structure. In fact, the proof of this result reveals that the rectangle is seen as a thick line of singularity points. The thinner the tubular structure, the finer the scale a should be, but the two quantities should maintain qualitatively the relation $a > 4r$, indicating that Directional Ratio can detect singularities without having to force the scale $a \to 0$.

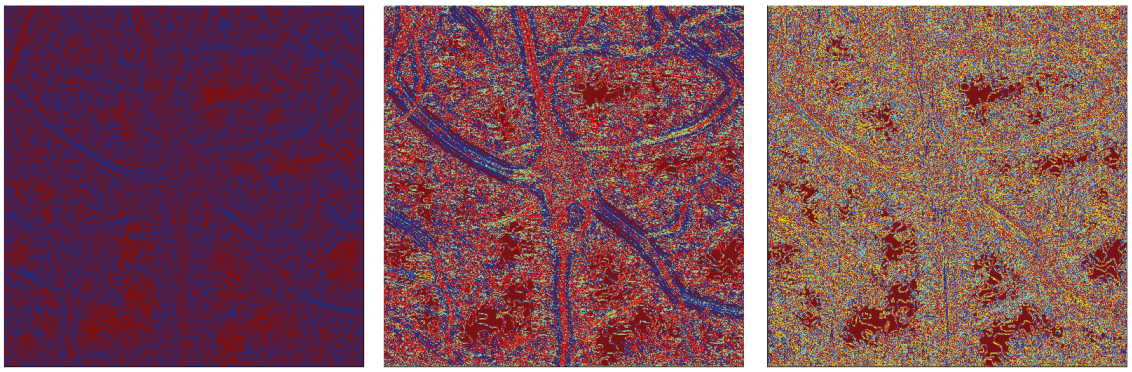

Figure 2.6: Values of directional ratio (color-coded) computed at various discrete scales; from left to right: $2^{-4}2^{\frac{1}{4}}$, $2^{-3}2^{\frac{1}{4}}$, and $2^{-1}2^{\frac{1}{4}}$. As the scale becomes coarser, the values of the directional ratio in the interior of neurites become consistently more uniform and do not exceed a certain low threshold, whose existence is predicted by Theorem 2.7. In the interior of the soma and of thicker neurites, the values of directional ratio vary wildly, once again as predicted, see Remark 2.8

.

Proposition 2.10 below indicates that the function $\mathcal{D}_a$ is weakly differentiable.

Let us now turn our attention to the weak differentiability of the directional ratio of $f \in L^1(R^2) \cap L^2(R^2)$, f can be a cartoon-like image. Without loss of generality, we take

$||f||_1 = 1$. To establish that $\mathcal{D}_a f$, given by the ratio (2.5), satisfies a Lipschitz condition, it is enough to verify this property for the numerator and the denominator of that ratio. To control how small the denominator can become, we assume that in an open set, Ω, there exists $\alpha > 0$ such that $|\mathcal{SH}_\psi f(a, s, y)| > \alpha$ for all $y \in \Omega$. Select $y \in \Omega$ and a vector h such that $y + h \in \Omega$. Using the triangle inequality, we have

$$|\langle f, T_{y+h}\psi^{(v)}_{a,s,0}\rangle| \leq |\langle f, T_y\psi^{(v)}_{a,s,0}\rangle| + |\langle f, (T_h - I)\psi^{(v)}_{a,s,0}\rangle|,$$

for every scale a and shear variable s. A similar inequality holds for horizontal shearlets. We will assume Ω to be convex. Since the Fourier transforms of $\psi^{(v)}$ and $\psi^{(h)}$ are C^∞ and compactly supported, the $\psi^{(v)}$ and $\psi^{(h)}$ are in the Schwartz space. Hence, all of their partial derivatives are uniformly bounded.

By applying the Mean Value Theorem of differential calculus, we obtain that

$$\begin{aligned} |\langle f, (T_h - I)\psi^{(v)}_{a,s,0}\rangle| &= \left| \int_{\mathbb{R}^2} f(x)(\psi^{(v)}_{a,s,0}(x-h) - \psi^{(v)}_{a,s,0}(x))dx \right| \\ &\leq \int_{\mathbb{R}^2} |f(x)||\psi^{(v)}_{a,s,0}(x-h) - \psi^{(v)}_{a,s,0}(x)|dx \\ &\leq C||f||_1\|h\|, \end{aligned}$$

where C is a constant derived by the L^∞-bounds of the partial derivatives of the horizontal and vertical shearlets. Since the shear variable s is taken in $[-1, 1]$, the constant C holds uniformly in s. Therefore, for every $s \in [-1, 1]$ we have that

$$|\langle f, T_{y+h}\psi^{(v)}_{a,s,0}\rangle| \leq \sup_s\{|\langle f, T_y\psi^{(v)}_{a,s,0}\rangle|\} + C||h|| \leq \sup_{s\in\mathbb{R}}\{|\mathcal{SH}_\psi f(a, s, y)|\} + C\|h\|.$$

By combining horizontal and vertical shearlets, we deduce that

$$\sup_{s\in\mathbb{R}}\{|\mathcal{SH}_\psi f(a,s,y+h)|\} \leq \sup_{s\in\mathbb{R}}\{|\mathcal{SH}_\psi f(a,s,y)|\} + C\|h\|.$$

By swapping the points y and $y+h$ in the previous inequality, we obtain that

$$|\sup_s\{|\mathcal{SH}_\psi f(a,s,y)|\} - \sup_s\{|\mathcal{SH}_\psi f(a,s,y+h)|\}| \leq C\|h\|$$

On the other hand, a similar argument establishes that

$$|\inf_s\{|\mathcal{SH}_\psi f(a,s,y)|\} - \inf_s\{|\mathcal{SH}_\psi f(a,s,y+h)|\}| \leq C\|h\|$$

Combining these two observations, we derive the following result.

$$\begin{aligned}
&|\mathcal{D}_a f(y+h) - \mathcal{D}_a f(y)| \\
&= \left|\frac{\inf_s\{|\mathcal{SH}_\psi f(a,s,y+h)|\}}{\sup_s\{|\mathcal{SH}_\psi f(a,s,y+h)|\}} - \frac{\inf_s\{|\mathcal{SH}_\psi f(a,s,y)|\}}{\sup_s\{|\mathcal{SH}_\psi f(a,s,y)|\}}\right| \\
&\leq \frac{|\inf_s\{|\mathcal{SH}_\psi f(a,s,y+h)|\} - \inf_s\{|\mathcal{SH}_\psi f(a,s,y)|\}|}{\sup_s\{|\mathcal{SH}_\psi f(a,s,y+h)|\}} \\
&+ \frac{|\sup_s\{|\mathcal{SH}_\psi f(a,s,y)|\} - \sup_s\{|\mathcal{SH}_\psi f(a,s,y+h)|\}|}{\sup_s\{|\mathcal{SH}_\psi f(a,s,y+h)|\}} \frac{\inf_s\{|\mathcal{SH}_\psi f(a,s,y)|\}}{\sup_s\{|\mathcal{SH}_\psi f(a,s,y)|\}} \\
&\leq \left(\frac{C}{\alpha} + \frac{C}{\alpha}\right)\|h\|.
\end{aligned}$$

The above discussion yields the next statement:

Proposition 2.10. *Assume that, for every point y in the open and convex set $\Omega \subset \mathbb{R}^2$, there exists $\alpha > 0$ such that $|\mathcal{SH}_\psi f(a,s,y)| > \alpha$. Then the shearlet-based Directional Ratio, $\mathcal{D}_a f$, at scale a, restricted on Ω, satisfies a Lipschitz condition and, thus, it is weakly differentiable on Ω.*

The weak differentiability of $\mathcal{D}_a f$ follows from the fact that $\mathcal{D}_a f$ is absolutely continuous since it satisfies a Lipschitz condition.

Chapter 3

Applications and Numerical Experiments

This chapter presents ideas, methods and results published in our prior work [41].

The ability of neurons to form mature synapses and functional connections in culture is a fundamental property that has allowed the first milestone studies in molecular neuroscience. In recent years, improved neuronal culturing techniques combined with sophisticated fluorescence microscopy have significantly expanded the initial scope of *in vitro* studies. They are now instrumental tools for large-scale studies of cultured neuronal networks used to identify phenotypic changes induced by chemical or biological agents in the context of brain disease models. Yet, such revolution in the field has not been paralleled by adequate quantitative methods for neuronal feature detection, extraction, and analysis, limiting the potential throughput of *in vitro* models.

Automated identification of the primary components of a neuron and extraction of its sub-cellular features are essential steps in such quantitative studies. High-content screenings (HCS), for instance, require the identification and extraction of multiple morphological

features of neurons, such as soma shape and volume, neurite length, and branching properties. Such complex information, usually compiled from multi-channel fluorescence images, requires automated processing methods to handle large batches of data and establish a confident statistical basis for a reliable prediction model. With the rapid and widespread rise in the use of HCS in basic science settings, automated detection of cell compartments from fluorescent images is an area of very active research [34, 18, 26, 8].

In this chapter, we concentrate on the automated detection of soma location and surface morphology in fluorescent images of cultured neurons, a challenging problem that has special importance for several reasons. In particular, *in vitro* phenotypic screenings of large scale neuronal cultures for drug-discovery and biomarker identification frequently require to quantify spatial distribution and expression levels of analytes of interest inside the soma [47, 48]. In addition, the detection of soma locations is a critical step to compute the centerline trace and extract the graph representation of each individual neuron, since the location of the soma is the main vertex of such a graph [2, 1]. Furthermore, accurate extraction of soma's surface morphology is one of the most important characteristics for discriminating different types of neurons [50].

Of all sub-cellular components of a neuron, somas are among the most challenging to detect and segment automatically in fluorescence images, due to the lack of robust markers and the uneven distribution of fluorescence signals. Clearly both problems pose different challenges. Detection is easier than segmentation because it involves an identification of a subset of a soma region. Automated soma/cell detection methods in many image analysis packages rely on contrast enhancement and image intensity thresholding [42, 54] and attempt the identification of somas by generating binary masks. These methods can be quite effective in phase-contrast microscopy [54, 13], but extension of these methods to images captured by other types of microscopy is difficult. In fluorescence imaging, the signal-to-

noise ratio is typically much lower. Furthermore, in neuronal cultures, somas are usually visible with the aid of the microtubules associated protein 2 (MAP2) antibody staining or nuclei markers (such as DAPI (4',6-diamidino-2-phenylindole) or TROPO-3), neither of which are soma-selective. The MAP2 protein is diffusely distributed in the somato-dendritic compartment and, as a result, MAP2 masks include both somas and dendrites. Nuclear staining, on the other hand, targets only nuclear DNA and excludes the cytoplasmic region of the soma surrounding the nucleus.

This limited combination of biological markers akin to somas and fluorescent microscopy channels dictate the need to develop image specific methods. Thus, several methods have been proposed to process images in which somas and other structures exist in the same fluorescence channel. Some of these methods use combinations of smoothing and morphological operators [2, 21, 52] or specialized filters such as the Laplacian-of-Gaussian (LOG) [3] and can be rather effective to detect somas in 2D. However, these types of methods have varying performance since they are very sensitive to the irregularities of the fluorescence signal and have proven to be either impractical or inefficient to extend to 3D. In particular, the use of LOG to detect local maxima of the fluorescence intensity signal, can lead to a high degree of false positives due to the irregular intensity profiles, causing detection of more than one soma candidate within a given neuron. To address these limitations, several ideas have been proposed, such as the detection of the soma area in the three 2D orthogonal projection images of the original 3D image stack using 2D morphological closing [1]. Notably, the algorithm recently proposed by [58] that, in addition to combining smoothing, morphological operators, and adaptive thresholding to detect the soma volume from the 2D orthogonal projection images, applies an ingenious variant of the Rayburst sampling method [44] to capture the surface of the soma.

None of those methods, though, are directly applicable to the type of imaging data

which are the preferred platform for HCS. Confocal images of neuronal cultures used for HCS typically consist of stacks containing 15-30 images, so that the 'data cube' is very thin along one of its axes: only 15-30 pixels are available along the z-direction, as compared with the x and y directions where the typical length can be 512 pixels or more. As a result, it is inefficient or even impossible to process these sets of data as true volumes using conventional 3D filters or adapting some of the ideas mentioned above. For example, the 2D orthogonal projections into the planes containing the z axis would not be very informative for the detection of the soma volume, due to the lack of a sizeable z dimension. An additional challenge is that, due to the acquisition process, in cultured neuronal images, the contrast changes significantly along the stack and reduces very rapidly on the optical slices that are farther away from the light source.

To address these challenges, in this chapter, we introduce an innovative method for the automated detection and accurate segmentation of somas from high-resolution confocal images of cultured neurons. Our approach includes an algorithm for the 2D analysis. However, this approach could be adapted for the 3D analysis. Due to the difficulty in processing confocal imaging data as true volumes, it is customary to convert the MAP2-stained confocal image stacks into 2D images by projecting the stacks along the z-axis. Consistently, our soma detection algorithm is designed to deal with these types of 2D images. Our approach includes an SVM-based segmentation routine to separate the neurons from the background, followed by a dedicated routine to separate the somas from the neurites. The routine combines the concept of Directional Ratio presented in Chapter 2 with variational methods. This approach enables very accurate detection of the somas in 2D, including the separation of clustered or contiguous somas.

3.1 2D Soma Segmentation

Our algorithm for 2D soma detection is applied on 2D images obtained by projecting a confocal image stack (comprising typically about 15-30 optical sections) along the axis perpendicular to the image plane (the z axis). This 3D-to-2D conversion is common in manual or semi-manual analysis of neuronal cultures. The most common projections are the *average intensity projection* (AIP) that outputs an image, wherein, each pixel stores average intensity over all images in the stack at a corresponding pixel location and the *maximum intensity projection* (MIP), that creates an output image where each of the pixels contains the maximum value over all images in the stack at the particular pixel location.

Our algorithm follows the procedure shown in Figure 3.1 and consists of the following steps: (1) a preprocessing routine to denoise the image; (2) a segmentation routine to separate the neurons from the background and to prepare the data for the next processing steps; (3) a routine that extracts the somas from the segmented images and includes Directional Ratio and level set routines; (4) a routine to separate those somas that are clustered together. The sections below will describe each one of these steps.

Image Preprocessing

The design of a highly efficient data preprocessing module is essential to take full advantage of the capabilities of instrumentation and enable accurate and robust processing of the acquired data. The preprocessing algorithm that we use in our image preprocessing step addresses the major source of degradation of confocal images: the noise introduced by the random nature of the photon-counting process at the detector, which can be modeled as a Poisson-distributed random process. To remove the noise, we apply the *shearlet shrinkage* denoising algorithm from [10, 38] that consists, essentially, of computing the shearlet

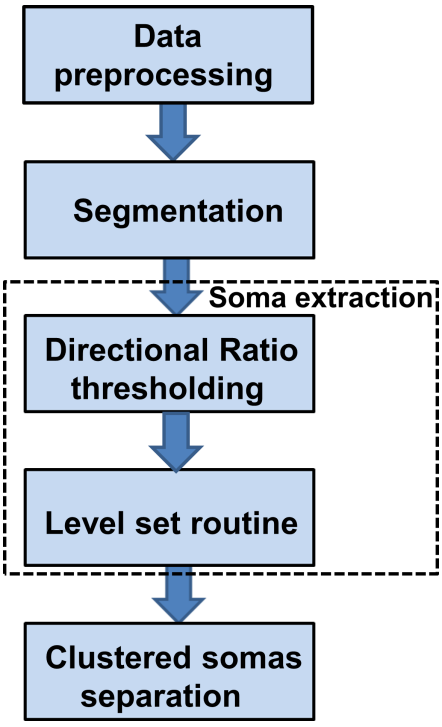

Figure 3.1: **Proposed algorithm for 2D soma detection.**

transform of the images, then applying a band-dependent threshold to the samples of the output values and, finally, computing the inverse shearlet transform. This algorithm is a refinement of the celebrated wavelet shrinkage algorithm and takes advantage of shearlets, a directional multiscale approach, that has optimally sparse representation properties for a large class of images [20, 31]. Thanks to these sparsity properties, this method is particularly efficient to remove noise without blurring edges [10, 12]. Overall, the boundaries of the structures in an image look sharper after the application of this denoising method.

Segmentation

In segmentation, we separate the neurons from the background. For this task, we adopted an algorithm recently developed by Jiménez et al. [27] that is based on support vector machines (SVMs) and whose main novelty is the use of features generated by a set of multiscale shearlet filters and isotropic Laplacian filters acting as self-steerable filters for a quick and efficient binarization of the axonal and dendritic structure [28, 29]. As is customary for many algorithms of this type, the proper classification stage of the algorithm is preceded by a training stage of the classifier. This is the most computationally-intensive part of the algorithm but needs to be run only once as long as the segmentation algorithm is applied to images of same type (e.g., same cell type and microscope setting). Then, the entire procedure is fully automated. We refer the reader to the references cited above for more details about the algorithm.

Soma Extraction

Our method to identify the soma within the segmented neuron uses the mathematical framework explained in Chapter 2. We use the result proven in Theorem 2.6. This

suggests that we can identify the somas with respect to the neurites, if we compute the Directional Ratio inside the already segmented neuronal structure at an appropiate scale. For the discrete implementation, we use a Haar-like function as an analyzing function which is compactly supported in a rectangle whose length is controlled by the scaling parameter and orientation is controlled by the rotation parameter.

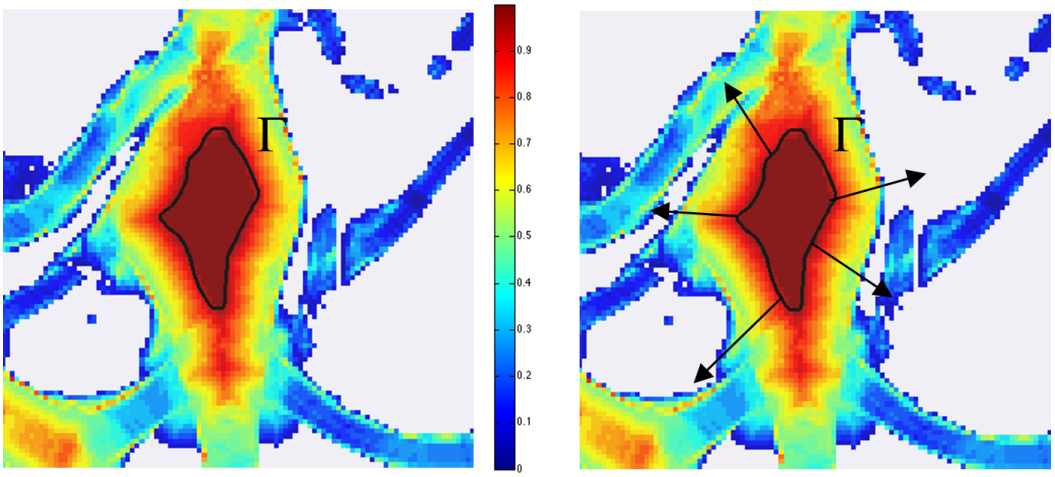

Figure 3.2: **Application of level-set method to detect soma area.** The figure shows a detail from a segmented image of a neuron (MIP) where colors correspond to the values of the Directional Ratio values and range between 1 (=red) and 0 (=blue). The application of the threshold value 0.9 identifies a region strictly inside the soma, with boundary curve Γ (in the left panel). The level set method evolves the boundary curve Γ with a velocity in the normal direction (indicated by the arrows in the right panel) that depends on the magnitude of the gradient of the Directional Ratio.

As we will show below in our numerical tests, when we compute the discrete Directional Ratio on segmented images of neuronal cultures, we observe very low values inside the neurites and much larger values (close to 1) inside the soma.(See Theorem 2.6) However, near the boundary of the soma, the Directional Ratio is low, due to the strong directionality induced by the boundary. As a result, the application of a threshold will allow us to identify a region *strictly inside the soma*, but not the entire soma. To detect the

entire soma including the region close to the boundary, we need to 'expand' the region we discovered using the method of the Directional Ratio. To achieve this, we apply a classical level-set method [39, 46].

Recall that the level set method is a variational approach introduced to track evolution of curves and shapes without having to parameterize these objects. The main idea is to identify a curve (or interface) Γ as the zero level set of a three-dimensional level set function ϕ and to follow the changes of $\Gamma = \{(x, y) : \phi(x, y) = 0\}$ from the evolution of ϕ. The motion of ϕ is determined by the *level-set equation*

$$\frac{\partial \phi}{\partial t} = v|\nabla \phi|,$$

where v is the speed of propagation of Γ in the normal direction. In our numerical tests, we will use the boundary curve of the region found by the Directional Ratio approach inside the soma as the initialization curve Γ of the level set evolution equation. We will set the speed of propagation of Γ in the normal direction proportional to $M - |\nabla (\mathcal{D}_a f)|$, where $\nabla (\mathcal{D}_a f)$ is the gradient of the Directional Ratio, pointing to the direction of the interior of the soma, and M is the maximum of the magnitude of the gradient of the Directional Ratio. This way, Γ evolves outwards, in the direction of the boundary of the segmented region (see Figure 3.2) and the velocity of evolution becomes slower and eventually stops when Γ reached the boundary of the segmented region. Note that, for our numerical implementation of the level-set method, we have adapted the implementation of Sumengen [49] based on [39].

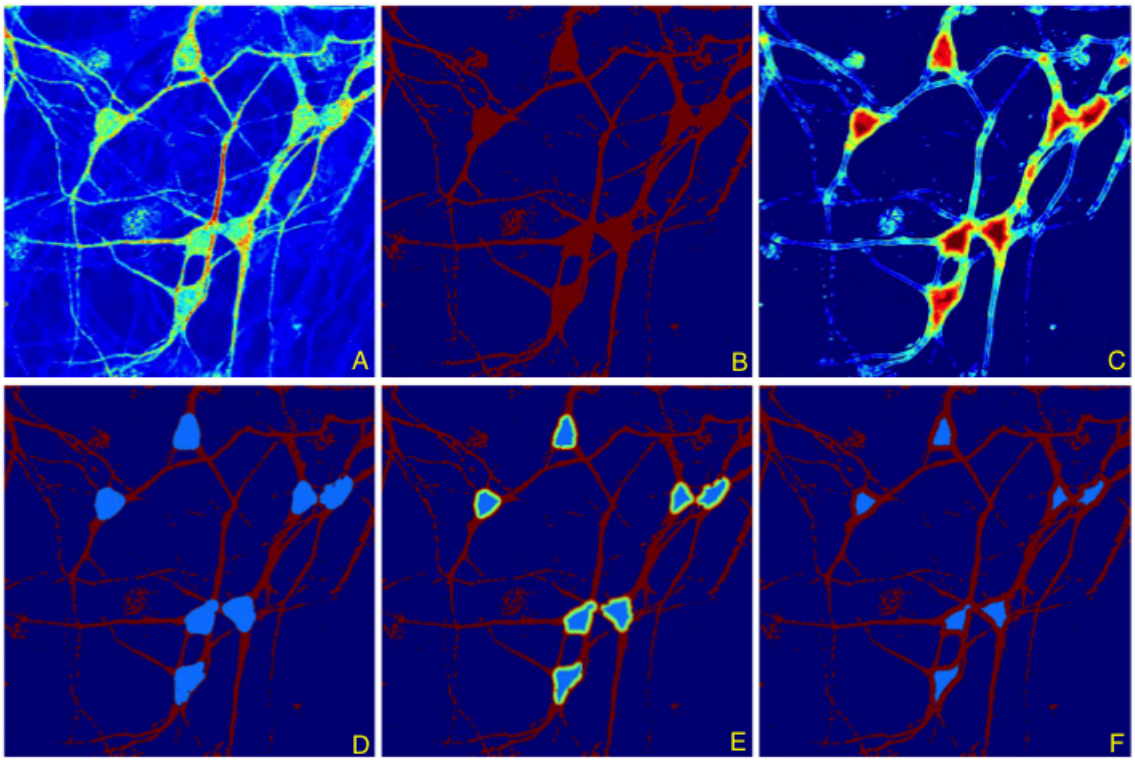

Figure 3.3: **Illustration of the pipeline of the 2D soma detection algorithm** (**A**) Denoised image, obtained using a shearlet-based denoising routine [10, 38]. (**B**) Segmented binary image. (**C**) Directional Ratio plot; the values range between 1, in red color (corresponding to more isotropic regions), and 0, in blue color (corresponding to more anisotripc regions); note that the Directional Ratio is only computed inside the segmented region, i.e., inside the red region in Panel B.(**D**) Soma detection, obtained by applying the level set method with the initialization curve determined by the boundary of points of local isotropy in each soma shown in Panel F.(**E**) Application of the level set method; showing soma region growing. (**F**) Detection of initial soma region, obtained by applying the threshold 0.9 to the values of the Directional Ratio in Panel C.

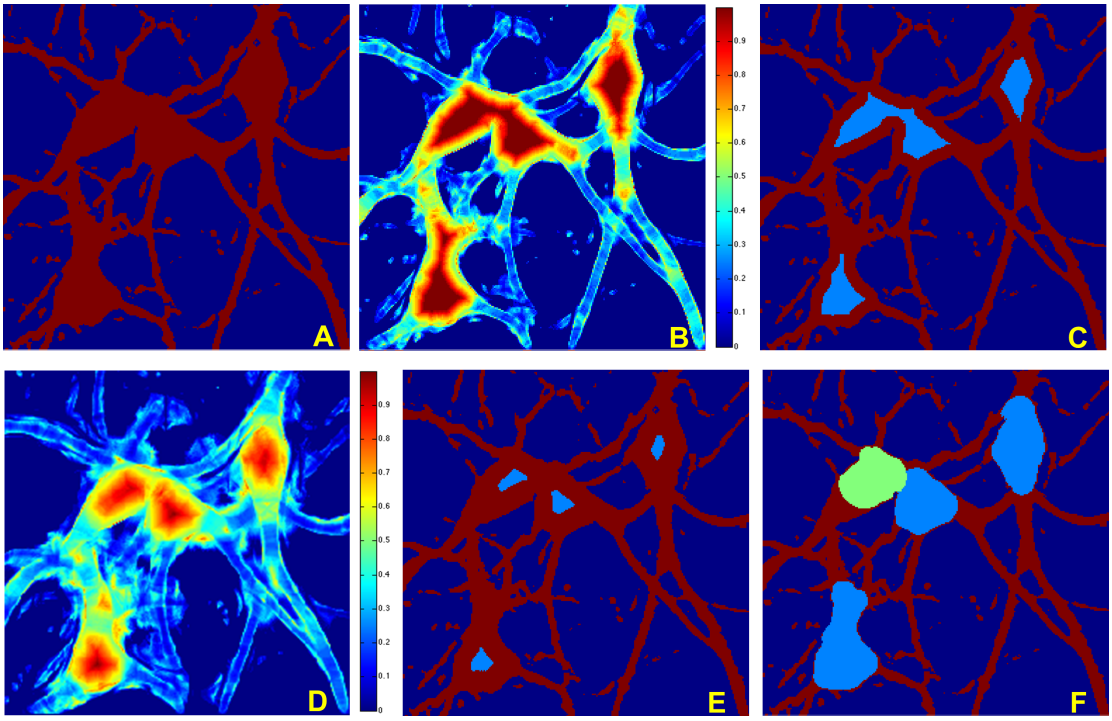

Figure 3.4: **Separation of clustered somas.** The figure illustrates the application of the multiscale Directional Ratio in combination with the level-set method to separate contiguous somas on the MIP of a confocal image of a neuronoal network culture. (**A**) Segmented image (detail). (**B**) Directional Ratio plot using directional filters of length 20 pixels (note that the diameter of a soma is about 40 pixels). (**C**) The blue region shows the points where the Directional Ratio exceeds the threshold 0.9, identifying the more isotropic region. (**D**) Directional Ratio plot using a directional filters of length 40 pixels; note that the larger values of the Directional Ratio are now concentrated within a smaller set inside the blob-like regions. (**E**) The blue region shows the points where the new Directional Ratio exceeds the threshold 0.9, identifying the more isotropic region; note that now there are two regions. (**F**): Soma detection obtained from the application of the level-set method, using the initialization curves determined by the boundary of the initial soma region in (**E**).

Separation of Clustered Somas

The method described above to separate somas from neurites in the segmented images of neuronal cultures may inadvertently segment multiple contiguous somas as a single soma. To address this issue, we designed a refinement of the soma extraction routine that proceeds as follows. After running our soma extraction routine, if the resulting soma area is too large (according to a criterion that we will describe below), we re-compute the Directional Ratio at a coarser scale, that is, by changing the scale parameter s_λ in such a way that the support of the analyzing functions are longer. By measuring the strength of the directional coherence at a coarser scale, the application of a threshold on the Directional Ratio will produce some smaller regions contained in the inner part of the segmented area. This is illustrated in Fig. 3.4, panel E. Next, similar to the above procedure, we apply the level-set method by using the boundary curves of these inner regions as the initialization curves of the level-set evolution equation. As the numerical test below will show, by propagating these curves until they touch each other, we are able to separate contiguous somas.

We still need to clarify how to determine whether the soma area detected by the algorithm is too large. This situation is interpreted as an indication that multiple somas appear in the MIP of the image as one contiguous soma region. In fact, we assume that somas in these images have similar surface areas (obviously, not similar shapes in general) and this observation applies to primary neuronal cultures which have fairly homogeneous populations. For instance, in our examples below the vast majority of neurons in the cultures derive from pyramidal-like principal cells. To separate these large regions into multiple contiguous somas, we assume that soma areas are normally distributed. In practice, we applied the Kolmogorov-Smirnov test to validate this assumption on a representative set of confocal images of neuronal cultures and found that our assumption is correct. Based

on this observation, we have used the 3σ rule as a criterion to identify regions containing multiple somas. That is, if the detected area differs from the expected soma area more than three times the estimated standard deviation, then we will conclude that the area contains two somas. Similarly, for the case of multiples contiguous somas, we can argue that if a detected area differs from N times the expected soma area more than three times the standard deviation, then we will conclude that the area contains $N + 1$ somas. In practice, however, we found that it is extremely rare to find more than two contiguous somas in typical fluorescence images of neuronal cultures. Yet, as we observed, the method that we described can be applied to multiple contiguous somas.

3.1.1 2D Soma Segmentation Matlab Algorithm

In this section, we present the 2D Soma Segmentation Matlab Algorithm to illustrate an application where we use the directional ratio concept in order to segment blob-like regions automatically. The input image of this step is the binary segmentation where the foreground structure (somas, dendritic branches, and axons) was separated from the background. We consider here 2D images computed as maximum projections of the original confocal image stacks (typically 10-20 slices). As shown in Flowchart 3.1, soma extraction is implemented in two steps: After computing the directional ratio for a certain scale and thresholding it (e.g. keep points whose directional ratio value is greater than 0.9), we derive a region inside the soma whose boundary is used to initialize a level-set routine. This area contains points of local isotropy at a certain scale. To find those regions, we apply a threshold close to 1 as predicted by Theorem 2.6, because these contain the points of local isotropy inside each soma at a given scale. Once somas are segmented the remaining part of the foreground corresponds to neurites (dendrites and axons). The identification inside

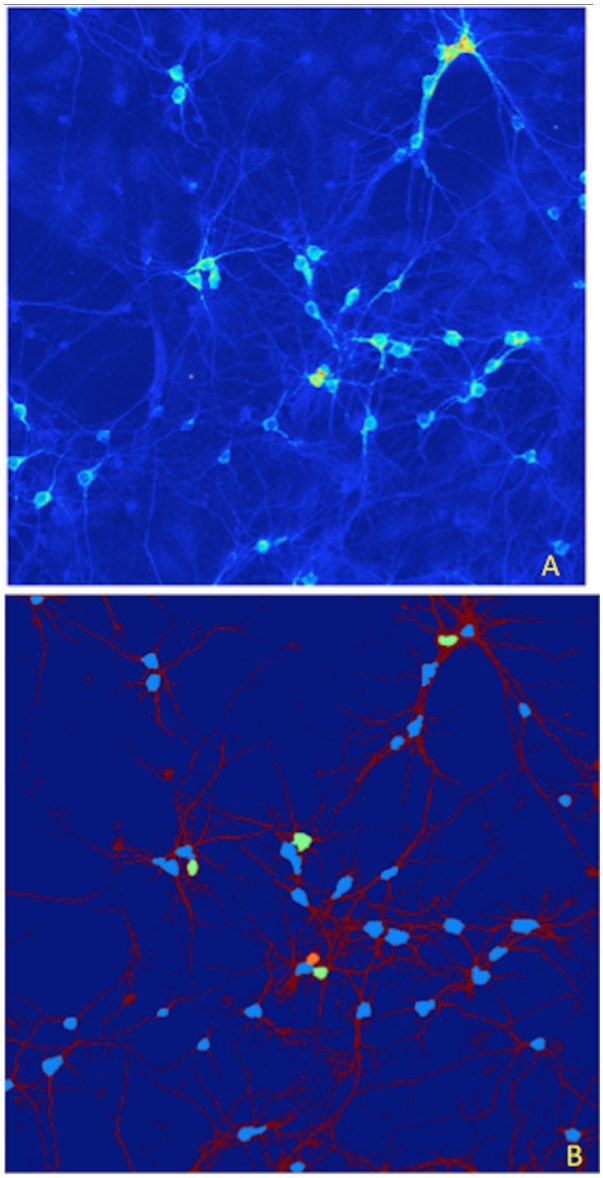

Figure 3.5: **Example of 2D soma detection and separation of clustered somas on large field-of-view image.** (**A**) Tiled and stitched confocal fluorescent image (MIP view) of a neuronal culture. Image size=1894 x 1894 pixels (1 pixel = 0.28 x 0.28μm). (**B**) Segmented binary image. Soma detection and separation of contiguous somas. Segmented neurites are shown in red color. Detected somas are shown in light blue; in case of contiguous somas, the separated somas appear in green and orange colors.

the foreground of regions of local isotropy at a certain scale also facilitate soma detections.

To compute directional ratio, we need to set the parameters used to generate the directional filters (molecules) $\chi_{s,r}$ in Algorithm 1. The algorithm is available at `www.math.uh.edu/~bozcan/research.html`. First, we choose the support size of directional filters according to the given segmented image. The images we consider are cultured neurons acquired under similar conditions. Therefore, their soma sizes have dimensions of the same order of magnitude and we can use *a single scale* to generate the directional filters. After some experimentation, we observed that choosing the correct length/scale $s/2$ and aspect ratio of the directional filters $\chi_{s,r}$ plays a crucial role in the accuracy of soma segmentation. If we choose $s/2$ less than the approximate radius of soma regions, we notice that the regions connecting soma and dendrites have high Directional Ratio. This increases false positives. On the other hand, if we choose $s/2$ larger than approximate radius of the soma regions, we notice that the size of the regions which have high directional ratio shrink excessively in a way that prevents the level set routine to properly identify soma boundaries. Therefore, we manually choose the directional filters to have a length equal to the approximate diameter of the soma in a segmented image. The radii of the somas in the images we experimented with is approximately equal to 20 pixels. Hence, we set the support size of the directional filters to be equal to 20 pixels. The main diagonal of each filter with the horizontal axis forms an angle equal to a multiple of ω selected to satisfy $\tan(\omega) = r/s$, the aspect ratio of the Haar-like filter. This equation determines the number of rotations of those directional filters because we set $\omega = \dfrac{\pi}{2N}$. We select a number of rotations, N, sufficient enough to cover a 90-degree angle. Since, as we increase the number of rotations, we better approximate the perpendicular filter to $\chi_{s,r}$, we set aspect ratio to be equal to 0.1. Hence, we set the number of rotations to be equal to a least integer number exceeding $\frac{\pi}{2\arctan(r/s)}$. For the aspect ratio 0.1, N is approximately equal to 15.

The advantage of a small aspect ratio is that the more the number of the rotations of the Haar-like filter, the better the approximately perpendicular filter to $\chi_{s,r}$. This improves the sensitivity of Directional Ratio to the presence of tubular structures at the appropriate scale, because the numerator of $\mathcal{D}_s\chi_{S_0}$ achieves its minimum value when the axis of the tubular structure is perpendicular to the orientation of the Haar-like filter. After these remarks, we can present the soma segmentation in Algorithm 2.

Algorithm 1 Generate Haar-like Directional Filters and their Rotations

Require:

Set support size of directional (molecules) filters S and number of rotations N

Ensure:

Create filters

1: Calculate directions: $\theta_k = \frac{k\pi}{\mathrm{N}}$ where $k = 0, 1, ..., (\mathrm{N}-1)$
For each direction:

2: Calculate coordinates of four points: $p_1 = (\frac{\mathrm{S}}{2}\cos((k-\frac{1}{2})\frac{\pi}{\mathrm{N}}), \frac{\mathrm{S}}{2}\sin((k-\frac{1}{2})\frac{\pi}{\mathrm{N}}))$ and $p_2 = (\frac{\mathrm{S}}{2}\cos((k+\frac{1}{2})\frac{\pi}{\mathrm{N}}), \frac{\mathrm{S}}{2}\sin((k+\frac{1}{2})\frac{\pi}{\mathrm{N}}))$ and the reflections of p_1 and p_2 with respect to origin.

3: Create a rectangular mask: set the corner points of the rectangle points determined in the previous step. The filter is the indicator (characteristic) function of the rectangle.

To segment somas, we produce the gradient of directional ratio and we apply a standard level-set routine [49]. The next proposition proves why such a gradient exists in a weak sense for shearlets. The initial condition for this level-set problem is determined by the boundary of each region containing the points of local isotropy in each soma, that is, the points for which the Directional Ratio for a given scale take a value greater than 0.9.

Note that, in our implementation of the algorithm, the soma detection and separation of contiguous somas are processed automatically, without external intervention. Following the computation of Directional Ratio with filters of length 20 pixels (about 1/2 of a typical soma's diameter), if the criterion indicated above signals the presence of areas containing two somas, then the Directional Ratio is re-computed using the filter length of 40 pixels

Algorithm 2 Detect and Segment Somas

Require:
Haar-like directional molecule (filter) F and segmented image I

Ensure:
Find soma regions

1: Convolve image I with filter F and with rotations of filter F_r, call Output $= I * M$ where $M = \{F, F_r\}$
2: Calculate directional ratio $D := \min$ Output / $\max$ Output
3: Create a mask with points that have directional ratio $D > 0.9$
4: Apply the level set method routine [49] to get complete soma regions
Item list which we use as input in level set method routine:
Take the x-derivative of the directional ratio of the segmented image I, D, computed in step 2, set as xderivative.
Take the y-derivative of the directional ratio of the segmented image I, D, computed in step 2, set as yderivative.
set $M := max(sqrt(xderivative.^2 + yderivative.^2))$
FORCE := $M - sqrt(xderivative.^2 + yderivative.^2)$
CURVE to evolve := the boundary points of mask we generate in step 3
stopping criteria : stop if rate of growth is less than 0.2.

(about the diameter of a typical soma). This is illustrated in Figure 3.4.

3.2 Numerical Results

In this section, we illustrate the application of our soma detection algorithms on several confocal image stacks of neuronal cultures. For our tests, we considered several 'standard' field-of-view images in low-density neuronal cultures, as commonly used in phenotypic screenings of analytes for drug-discovery or biomarker identification. These images contain a relatively small number of neurons, typically about 5-10. We show below that our algorithm can automatically extract soma locations from any such image in about 40 seconds. However, processing time heavily depends on the efficiency of the level-set evolution routine. Faster routines will greatly improve the processing time. Note that a large

number of such images, usually 50-100 or more, need to be analyzed in studies like those in the cited literature. As we further explain later, our algorithms are scalable and can be applied without changes to larger images of neuronal cultures containing more neurons. To illustrate this capability we also show the application of the soma detection algorithm on a tiled and stitched large field-of-view image containing more than 40 neurons, Figure 3.5.

3.2.1 2D Soma Segmentation Results

We considered twelve image stacks with different sizes to test our 2D algorithm for soma detection. The stacks we considered comprise between 10 and 25 images each and contain a variable number of neurons, ranging between 1 and 8. From each stack, we generated the Maximum Intensity Projection (MIP) images. The resulting 2D images were processed by the algorithm as described in Section 3.1. Some representative results are shown in Figures 3.6 and 3.7. These figures illustrate the proprocessing, segmentation, and soma detection on images of size 512×512 pixels containing seven and eight somas, respectively. Figure 3.7 also illustrates the capability of the algorithm to separate contiguous somas.

3.2.2 2D Algorithm Validation

For the validation of the algorithm, we first tested the ability to identify the correct somas and separate the contiguous ones. The results are reported in Table 3.1 and show that the algorithm is able to correctly identify and separate the somas in all 12 confocal image stacks we used.

To quantitatively validate the performance of our algorithm on soma segmentation, we employed standard statistical measures of the performance of a binary classification test [4]

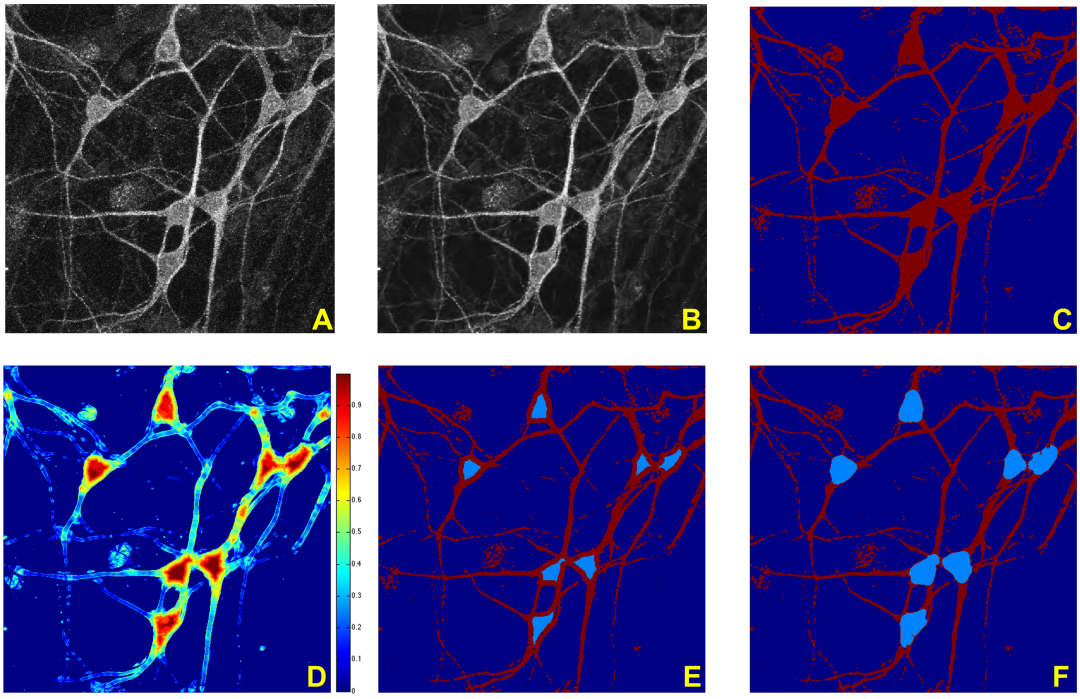

Figure 3.6: **Example of 2D soma detection.** (**A**) Original image, obtained by computing the maximum projection on the image stack. (**B**) Denoised image, obtained using a shearlet-based denoising routine. (**C**) Segmented binary image. (**D**) Directional Ratio plot; the values range between 1, in red color (corresponding to more isotropic regions), and 0, in blue color (corresponding to more anisotripc regions); note that the Directional Ratio is only computed inside the segmented region, i.e., inside the red region in Panel C. (**E**) Detection of initial soma region, obtained by applying a threshold to the values of the Directional Ratio in Panel D. (**F**) Soma detection, obtained by applying the level set method with the initialization curve determined by the boundary of the initial soma region in Panel E.

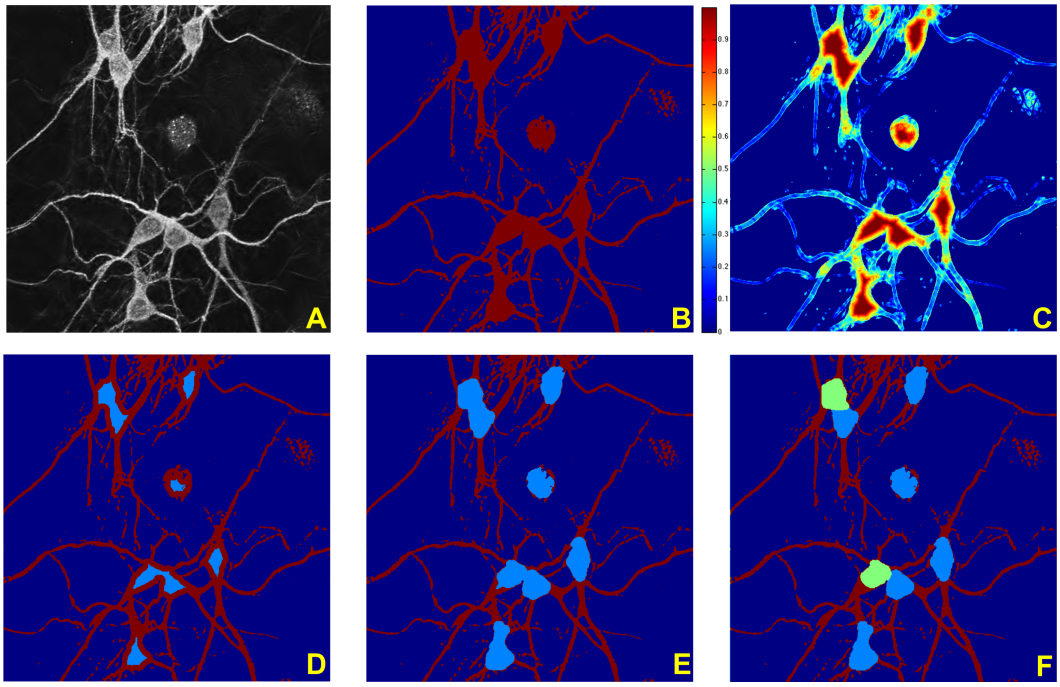

Figure 3.7: **Example of 2D soma detection.** (**A**) Denoised image, obtained using a shearlet-based denoising routine. (**B**) Segmented binary image. (**C**) Directional Ratio plot; the values range between 1, in red color (corresponding to more isotropic regions), and 0, in blue color (corresponding to more anisotripc regions); note that the Directional Ratio is only computed inside the segmented region, i.e., inside the red region in Panel B. (**D**) Detection of initial soma region, obtained by applying a threshold to the values of the Directional Ratio in Panel C. (**E**) Soma detection, obtained by applying the level set method with the initialization curve determined by the boundary of the initial soma region in Panel D. (**F**) Separation of contiguous somas; two regions from Panel E are recognized as too large and hence divided using the level set method.

whose definitions are as follows. The *True Positive Rate* TPR (also called *Sensitivity*) measures the proportion of correctly identified soma pixels with respect to the total number of true soma pixels, which are manually identified by a domain-expert . That is, denoting by TP (= true positive) the number of correctly identified soma pixels and by FN (= false negative) the number of true soma pixels incorrectly rejected, we define:

$$TPR = \frac{TP}{TP + FN}.$$

The *False Positive Rate* FPR measures the proportion of pixels incorrectly identified as soma pixels with respect to the total number of true soma pixels. That is, denoting by FP (= false positive) the pixels incorrectly selected as soma pixels, we adopt a special rate for the purposes of this work defined by

$$FPR = \frac{FP}{TP + FN}.$$

This rate is a penalty akin to wrong soma pixel detections. When our FPR is compared with the traditional FPR given by

$$FPR = \frac{FP}{TN + FP}.$$

we realize that the commonly used FPR is destined to be practically equal to zero because false soma detections are always in order-of-magnitudes less than the number of background voxels due to the inherent sparsity neuronal tissue in these images. Hence, we decided to introduce a new metric which express false soma detections as a percentage of

[0]The expert user manually identifies the somas in each image stack without knowledge of the algorithm results.

Stack	Soma number	Correct detection	False detection	Contiguous Soma Presence
Stack 1	7	7	0	No
Stack 2	6	6	0	Yes
Stack 3	7	7	0	Yes
Stack 4	8	8	0	Yes
Stack 5	4	4	0	No
Stack 6	7	7	0	No
Stack 7	5	5	0	No
Stack 8	1	1	0	No
Stack 9	2	2	0	No
Stack 10	2	2	0	No
Stack 11	4	4	0	No
Stack 12	5	5	0	No

Table 3.1: Validation of soma detections

soma volume measured in pixels/voxels. Finally, the *Dice Coefficient* DC (also called F1 score), that is used to compare the similarity between two samples or measures, is

$$DC = \frac{2\,TP}{2\,TP + FN + FP}.$$

Note that the denominator $2\,TP + FN + FP = TP + FP + FN + TP$ is the sum of the detected pixels and the true soma pixels.

The results reported in Tables 3.2, 3.3, 3.4, 3.5 show the True Positive Rate, False Positive Rate and Dice Coefficient for the somas shown in Figures 3.14 , 3.15. The results in the tables show that our method yields average TPR equal to 0.94, indicating that we get a very high proportion of true soma pixels; the value of the average FPR is 0.13, indicating that our approach tends to err on the side of false positives (i.e. we tend to over-segment). The average Dice coefficient is 0.90, indicating that the automated soma detection is very close to the manual segmentation overall.

To illustrate the capabilities of our approach on a larger field-of-view image, we applied

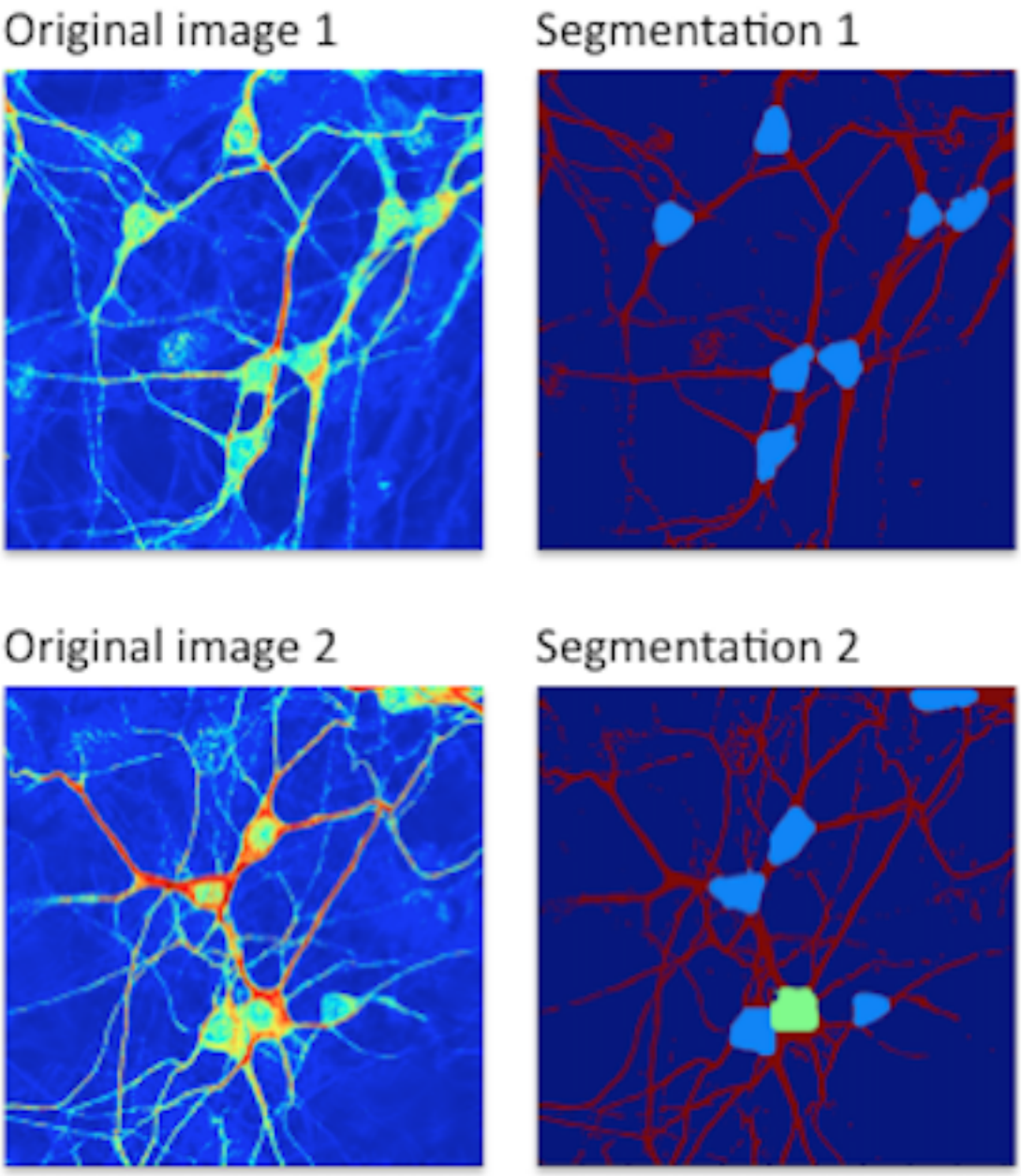

Figure 3.8: Illustration of soma detections given in Table 3.1

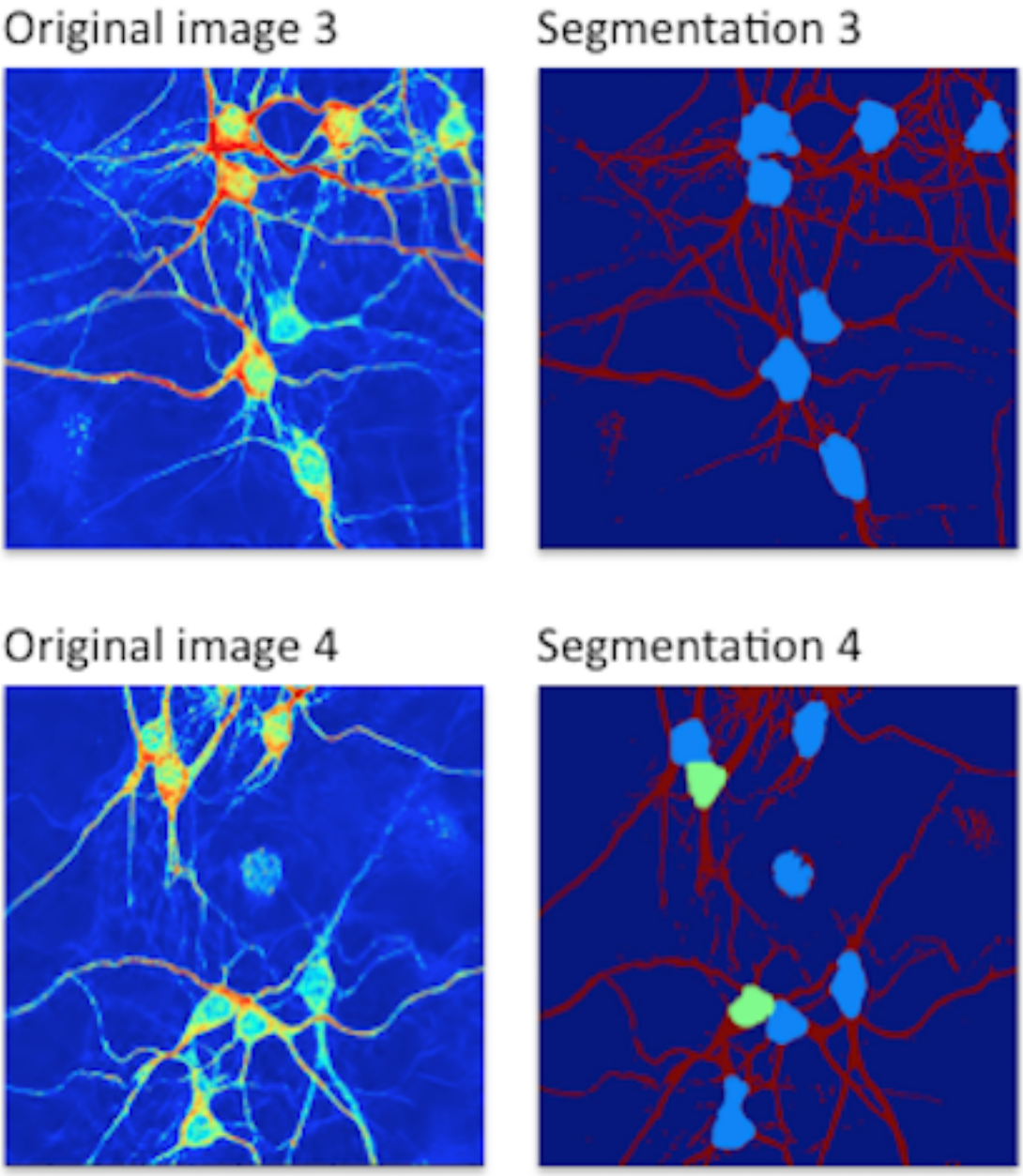

Figure 3.9: Illustration of soma detections given in Table 3.1

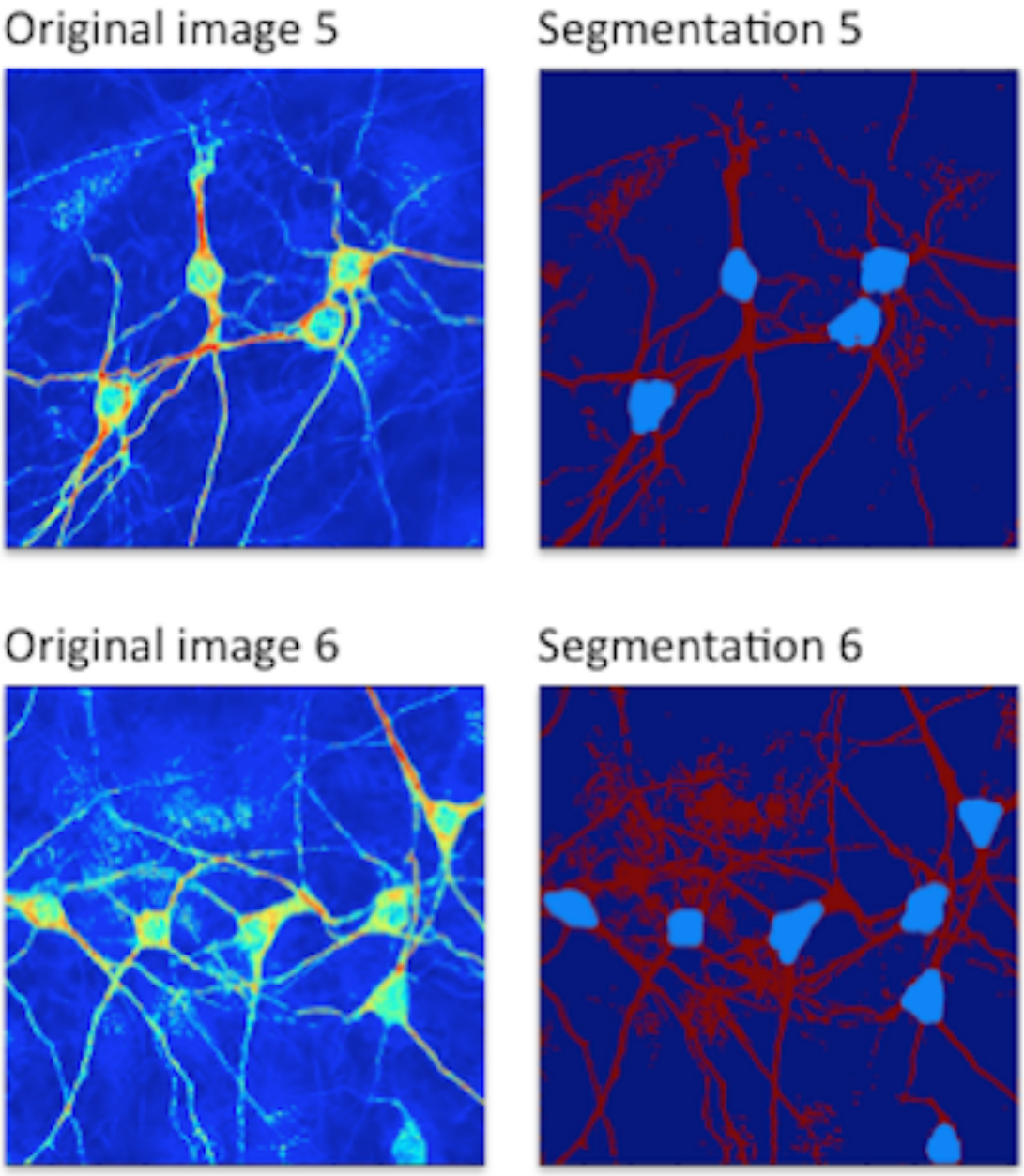

Figure 3.10: Illustration of soma detections given in Table 3.1

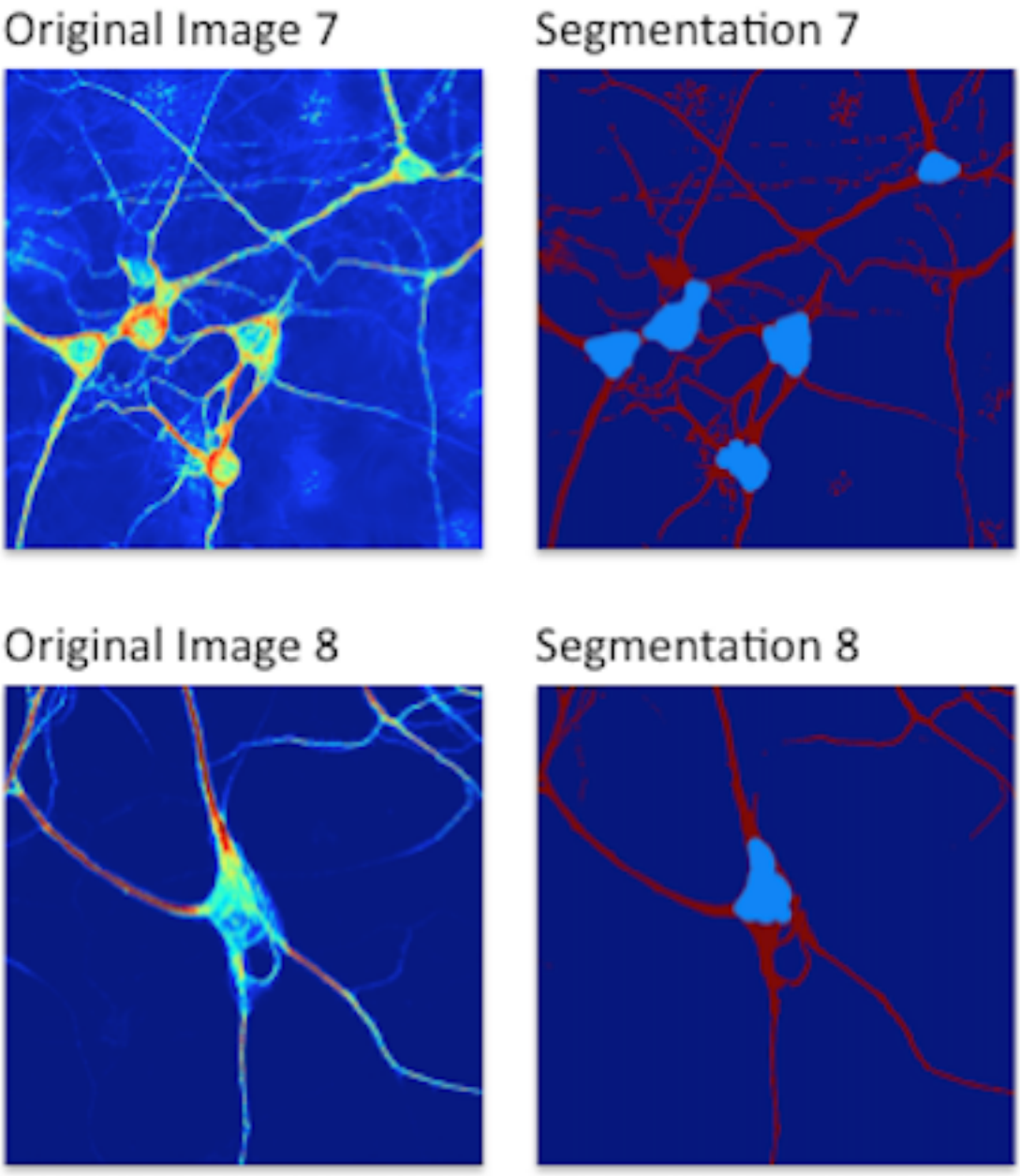

Figure 3.11: Illustration of soma detections given in Table 3.1

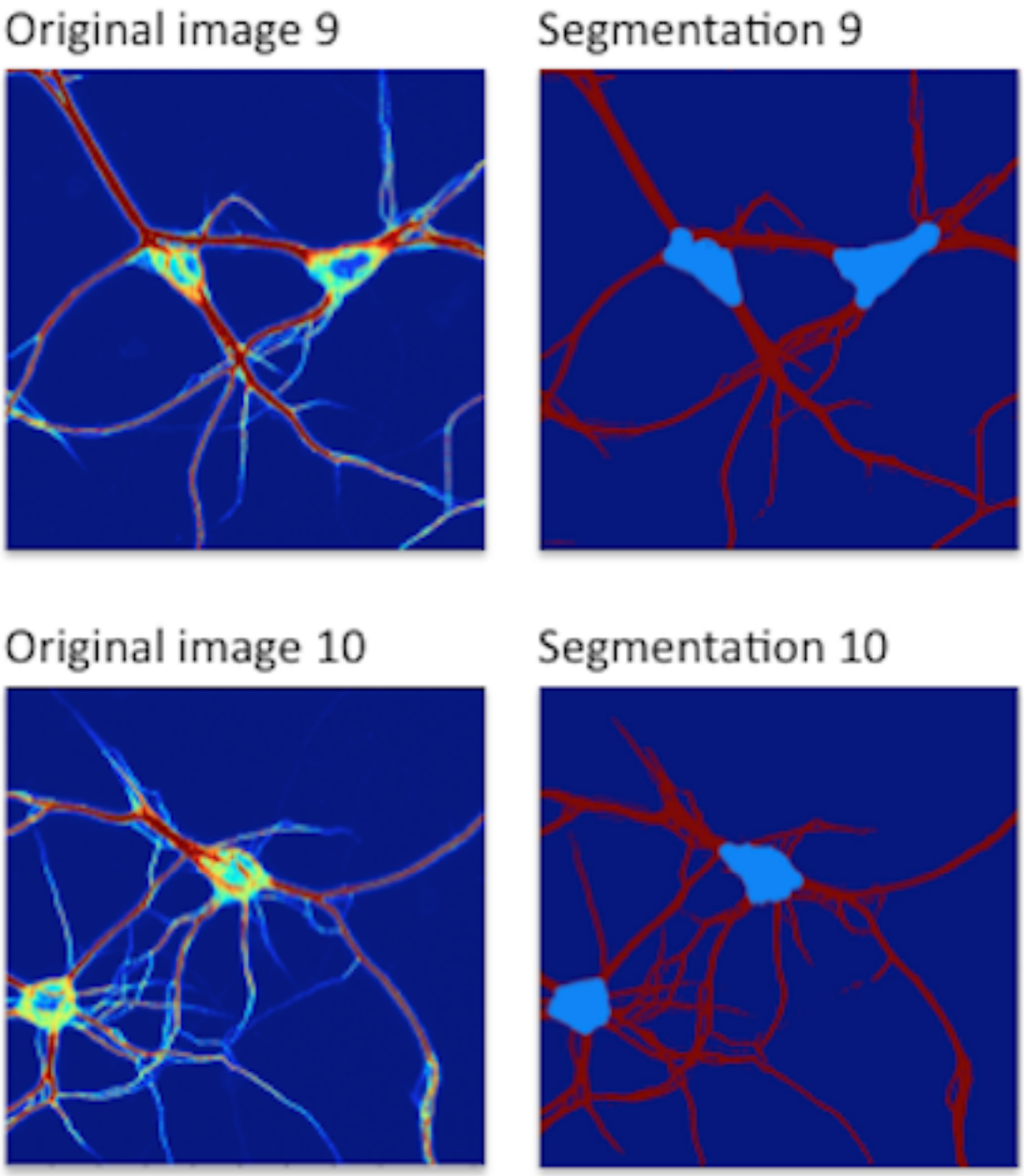

Figure 3.12: Illustration of soma detections given in Table 3.1

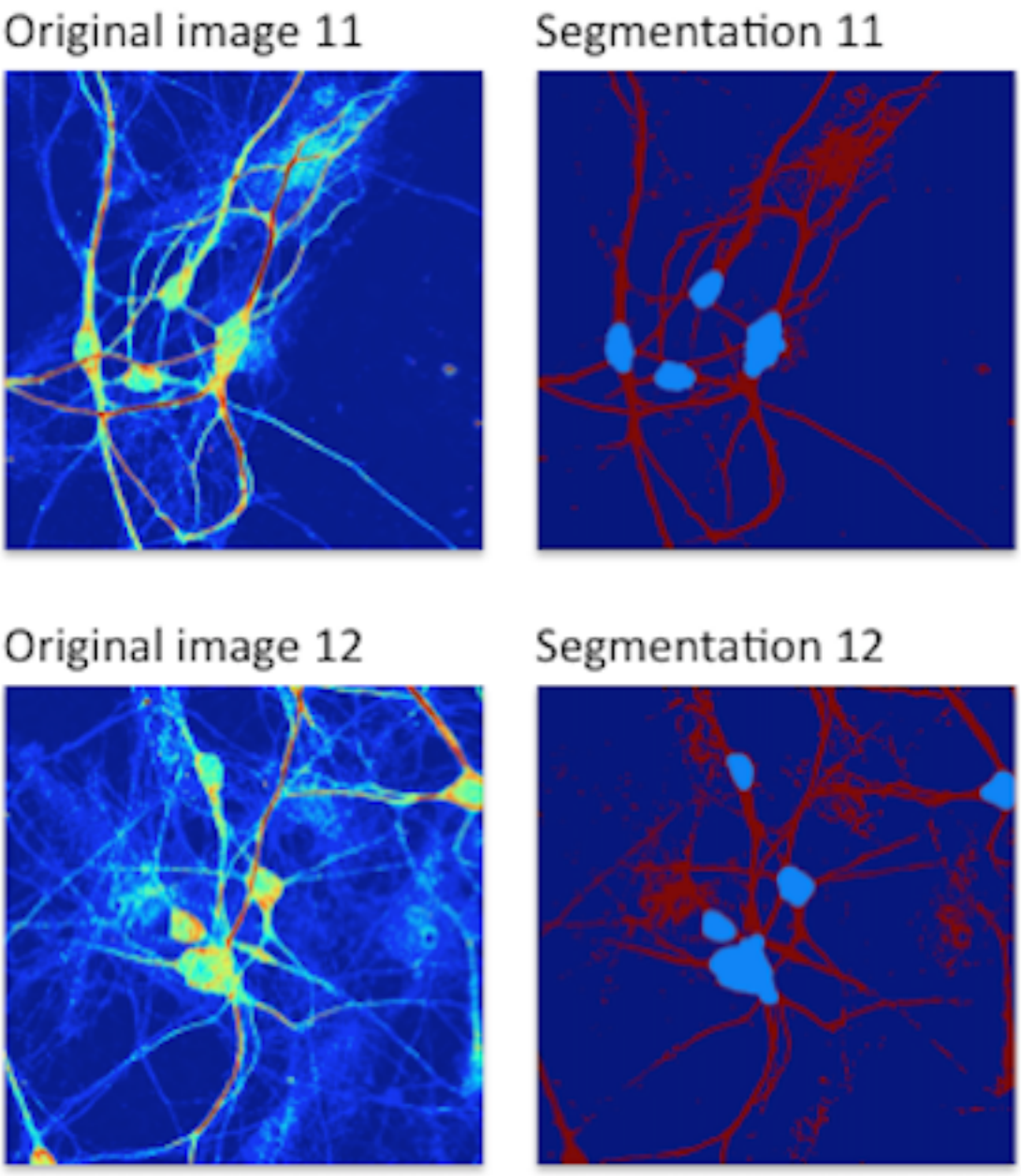

Figure 3.13: Illustration of soma detections given in Table 3.1

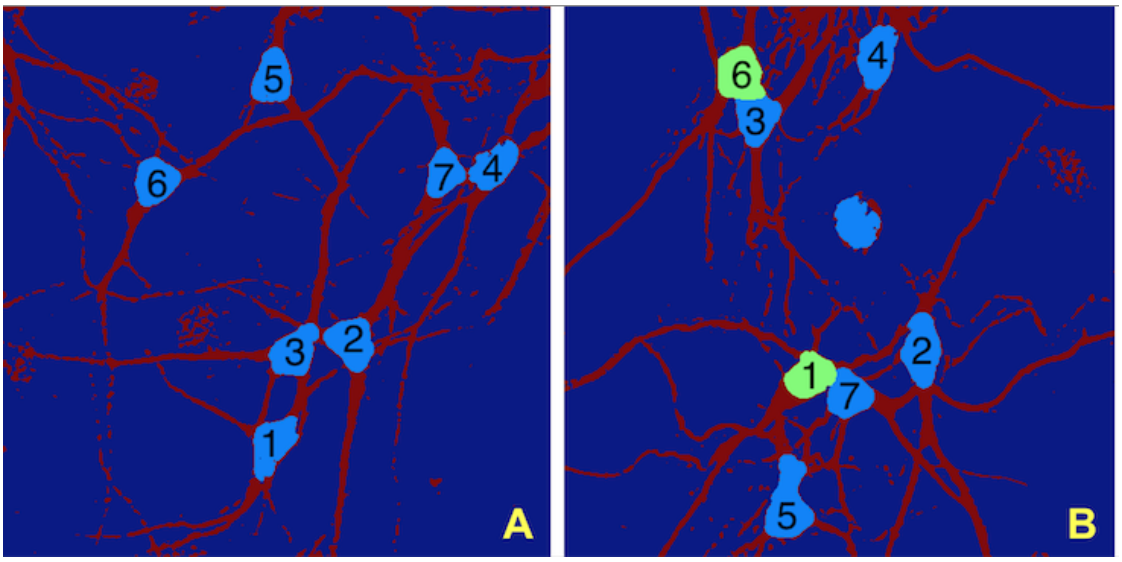

Figure 3.14: **Performance of soma segmentation.** Performance metric for the segmentation of the somas contained in these image are illustrated in Tables 2 and 3. (**A - B**) 2D-segmentation and soma detection on the MIP images of Figures 3.6 and 3.7, respectively.

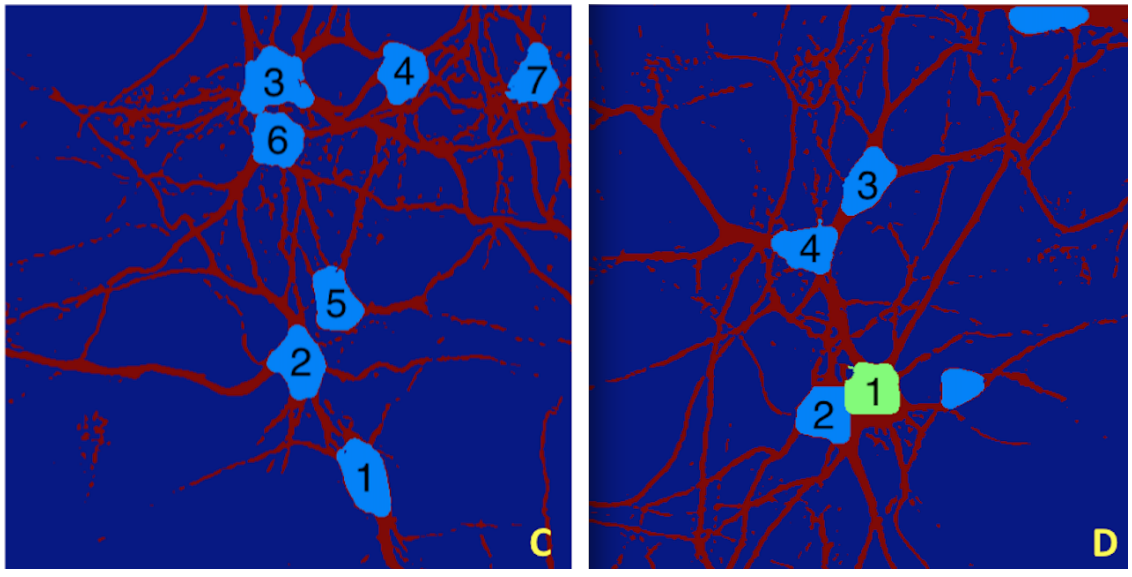

Figure 3.15: **Performance of soma segmentation.** Performance metric for the segmentation of the somas contained in these image are illustrated in Tables 4 and 5. (**C-D**) 2D-segmentation and soma detection on a similar MIP image.

Soma	TPR	FPR	DC
1	0.83	0.04	0.88
2	0.95	0.06	0.94
3	0.97	0.09	0.94
4	0.84	0.08	0.87
5	0.97	0.05	0.96
6	0.98	0.06	0.96
7	0.85	0.09	0.87
average	0.92	0.07	0.92

Table 3.2: Performance metrics results on soma segmentation of Figure 3.14, panel A.

Soma	TPR	FPR	DC
1	0.98	0.14	0.92
2	0.79	0.12	0.82
3	0.92	0.08	0.92
4	0.99	0.14	0.92
5	1	0.6	0.76
6	0.94	0.3	0.83
7	0.99	0.18	0.91
average	0.94	0.22	0.87

Table 3.3: Performance metrics results on soma segmentation of Figure 3.14, panel B.

Soma	TPR	FPR	DC
1	0.97	0.09	0.94
2	0.99	0.12	0.93
3	0.99	0.49	0.79
4	0.99	0.15	0.92
5	0.94	0.28	0.84
6	1	0.31	0.86
7	0.98	0.25	0.88
average	0.98	0.24	0.88

Table 3.4: Performance metrics results on soma segmentation of Figure 3.15, panel C.

Soma	TPR	FPR	DC
1	0.86	0.16	0.85
2	0.90	0.03	0.93
3	0.92	0.02	0.94
4	0.98	0.13	0.91
average	0.91	0.08	0.91

Table 3.5: Performance metrics results on soma segmentation of Figure 3.15, panel D.

our 2D soma-detection algorithm on a tiled and stitched large field-of-view image of size 1894×1894 pixels containing about 45 neurons. The soma detection and segmentation result is reported in Figure 3.5. The figure shows that our algorithm can reliably detect essentially all somas also in this larger image. Note that the soma detection algorithm is not expected to work for the somas overlapping the border of the image, as their shapes may be inconsistent with the model used by our method based on Directional Ratio. Our method is also very effective in separating contiguous somas, even though it fails in some cases. About the center of the Figure 3.5, three contiguous somas are correctly separated (shown in light blue, green and orange colors); however, in the top right region, where there is another set of three contiguous somas, the algorithm is only able to separate two of them. This is because the fact two of the three soma are rather small and the area they occupy is not recognized as a location of multiple somas.

3.3 Discussion

Methods we proposed for the automated detection of soma location and morphology in confocal images of neuronal cultures can be easily applied to image stacks larger than those considered in this thesis. The computational cost of our algorithms depends linearly on the size of the data, which is reasonable for most applications. Several standard methods can

be applied for speed improvement and management of larger data sets within the proposed framework.

The routines for denoising, in particular, rely on the discrete shearlet transform and their computational cost grows log-linearly with the data size [10, 55]. Recently, a parallel implementation of the discrete shearlet transform that uses a Graphic Processor Unit (GPU) was introduced and it was reported to achieve a 20-30 times speed improvement over the Matlab implementation used for the results reported in this thesis [15]. This implementation can easily be adapted to our algorithm since it implements the same shearlet decomposition used in this thesis and the code is publicly available.

The main computational cost of our algorithms is due to the routine for the soma segmentation that applies a level set method and it requires the numerical solution of a partial differential equation. Also for this routine, a GPU implementation was proposed [6] that could be adapted to achieve computational speed improvement.

Parallelization is also a valuable strategy for reducing computational time in our algorithm. The level-set method can be applied in parallel for each soma, following the application of the Directional Ratio routine. However, the Directional Ratio routine must be computed for each image in a stack, in order to identify soma locations and possible contiguous somas.

The performance of our algorithms critically depends on the segmentation routine since the soma area is found *within* the segmented region. Any pixels discarded during the segmentation will not be classified as soma pixels. Despite this potential weakness, we found that the segmentation routine is very reliable for the type of data we consider, as one can conclude by observing the performance metric results showing consistently high values for the True Positive Rate. Consequently, we consistently identify pixels in neurites with high accuracy during segmentation. On the other hand, the performance metric tables show that

even with respect to the very penalizing FPR used, we score reasonably low values of False Positives. However, in some cases, this penalizing FPR tends to be relatively as high as 24% of the soma spatial extend indicating that, in general, we tend to positively identify a non-negligible number of pixels that are not in the soma. We attribute the main cause of this type of error to the level-set method and, more precisely, the to fact that the level-curve propagated by the evolution equation does not always stop within the soma. For example in the detection of soma 5 in Figure 3.14, Panel B and soma 3 in Figure 3.14, Panel C, we measure large values of FPR because the level-set curve is propagated beyond the soma and partially inside the neurites. Note that, in these cases, the shape of the somas are not very round and the neurites emerging from the somas are not very thin, making the it rather difficult to establish where soma ends and neurites start. Nevertheless, we think that it is possible to refine the algorithm in order to control this error in future work. For example, we could introduce a constraint or a penalty term in the level-set routine to ensure that the detected soma region does not become too elongated.

Even though our algorithms were designed with the goal to process confocal images of neuronal cultures, some of our ideas are applicable to other types of imaging data. In particular, the segmentation routine was already tested on other confocal image stacks [28] and it is expected to work on brightfield microscopy images as well. Similarly the method of Directional Ratio is expected to work with other types of imaging data, even though we did not conduct specific tests.

3.4 Computational Efficiency, Hardware and Software

We implemented the numerical codes for the proposed method using MATLAB 7.12.0 (R2011a). The tests for the 2D soma-detection were performed using a MacBook with

Intel Core i7 2.66 GHz and 4 GB RAM. Even though we did not optimize the computational efficiency of the routines, the computation times were very reasonable. On a 2D image of size 512×512 pixels, the average computational time for the shearlet-based denoising is approximately 11 seconds; the average computational time for the 2D segmentation routine is approximately 8 seconds; the computational time of the Directional Ratio routine that is used to initialize the soma detection depends slightly on the choice of parameters (number of directional bands and filter length) and it ranges between 0.2 and 0.6 seconds; the average computational time for the level-set method implementation and completion of soma segmentation is about 30 seconds. In our tests, we used 12 directional filters. Matlab routines for shearlet denoising and Directional Ratio are available at `www.math.uh.edu/~dlabate/software.html`. As mentioned above, we use the level-set method implementation of Sumengen [49].

3.5 Conclusion

We have introduced a novel method for the automated detection of soma location and morphology in confocal images of neuronal cultures. In addition to the usual difficulties associated with processing fluorescent images, this problem presents the additional challenge that this type of confocal image stacks usually contain a small number of images (about 15-25). Consequently, only a small number of pixels is available along the z-direction and the use of standard 3D filters to process the data volume is inefficient or impractical. The approach we developed addresses these challenges by relying on a number of innovative ideas and techniques ranging from Fourier Analysis and differential equations to statistics and computer vision. Accurate extraction of the somas in MIP images is achieved using an SVM-based segmentation routine combined the Directional Ratio algorithm and a level-set

method. This approach is also applied to reliably and efficiently separate contiguous somas in MIP images.

Automated detection and segmentation of somas in confocal images of neuronal cultures is a fundamental analytical tool not only for the identification and discrimination of neurons but more generally for the detection, analysis and profiling of complex phenotypes from cultured neuronal networks. Methods proposed and illustrated in this thesis will facilitate the development of a high-throughput quantitative platform for the study of neural networks for applications including High Content analysis which our group is currently pursuing.

Bibliography

[1] Al-Kofahi Y., Dowell-Mesfin N., Pace C. et al., *Improved detection of branching points in algorithms for automated neuron tracing from 3D confocal images*, Cytometry A, Volume 73, 2008, pp. 36-43

[2] Al-Kofahi K. A., Lasek S., Szarowski D. H. et al., *Rapid automated three-dimensional tracing of neurons from confocal image stacks*, IEEE Transactions on Information Technology in Biomedicine, Volume 6, 2002, pp. 171-187

[3] Al-Kofahi Y., Lassoued W., Lee W. and Roysam B., *Improved automatic detection and segmentation of cell nuclei in histopathology images*, IEEE Transactions on Biomedical Engineering, Volume 57, 2010, pp. 841-852

[4] Altman D. G., Bland J. M., *Diagnostic tests. 1: Sensitivity and specificity,* British Medical Journal, Volume 308, Number 6943, 1994, pp. 1552

[5] Candès E. J., Donoho D. L., *New tight frames of curvelets and optimal representations of objects with piecewise* $\mathbb{C}^2$ *singularities*, Communications on Pure and Applied Mathematics, Volume 56, 2004, pp. 216-266

[6] Cates J. E., Lefohn A. E., Whitaker R. T., *GIST: An interactive GPU-based level-set segmentation tool for 3d medical images*, Journal on Medical Image Analysis, Volume 8, 2004, pp.217-231

[7] Coifman R.R., Weiss G., *Littlewood-Paley and multiplier theory*, Bulletin of the American Mathematical Society, Volume 84(2), 1978, pp. 242-250

[8] Cornelissen F., Verstraelen P., Verbeke T. et al., *Quantitation of chronic and acute treatment effects on neuronal network activity using image and signal analysis: toward a high-content assay*, Journal of Biomolecular Screening. Volume 18, 2013, pp. 807-819

[9] Donoho D. L., *Sparse components of images and optimal atomic decomposition*, Constructive Approximation, Volume 17, 2001, pp. 353-382

[10] Easley G. R., Labate D., Lim W., *Sparse directional image representations using the discrete shearlet transform*, Applied and Computational Harmonic Analysis, Volume 25, 2008, pp. 25-46

[11] Easley G. R., Labate D., Patel V., *Directional multiscale processing of images using wavelets with composite dilations*, Journal of Mathematical Imaging and Vision, Volume 48(1), 2014, pp. 13-34

[12] Easley G. R., Labate D., *Image processing using shearlets*, Applied Numerical Harmonic Analysis, Birkhäuser Boston, 2012, pp. 283–325

[13] El-Laithy K., Knorr M., Ks J., Bogdan M., *Digital detection and analysis of branching and cell contacts in neural cell cultures*, Journal of Neuroscience Methods, Volume 210, 2012, pp. 206-219

[14] Frangi A. F., Niessen W. J., Vincken K. L., Viergever M. A., *Multiscale vessel enhancement filtering*, Springer Verlag, Berlin, 1998, pp. 130-137

[15] Gibert X., Patel V., Labate D., Chellappa R., *Discrete shearlet transform on GPU with applications in anomaly detection and denoising*, EURASIP Journal on Advances in Signal Processing, Springer International Publishing, 2014

[16] Gonzalez G., Fleuret F., Fua P., *Learning rotational features for filament detection*, International Conference on Computer Vision and Pattern Recognition, 2009

[17] Gonzalez G., Fleuret F., Unser M., Fua P., *Steerable features for statistical 3D dendrite detection*, International Conference on Medical Image Computing and Computer Assisted Intervention, 2009

[18] Gough A. H., Johnston P. A.,*Requirements, features, and performance of high content screening platforms*, Methods of Molecular Biology., Volume 356, 2007, pp. 41-61

[19] Guidotti P., Longo K., *Two enhanced fourth order diffusion models for image denoising*, Journal of Mathematical Imaging and Vision, Volume 40(2), 2011, pp. 188-198

[20] Guo K., Labate D., *Optimally Sparse Multidimensional Representation Using Shearlets*, SIAM Journal on Mathematical Analysis, Volume 39, 2007, pp. 298-318

[21] He W., Hamilton T. A., Cohen A. R. et al., *Automated three-dimensional tracing of neurons in confocal and brightfield images,* Microscopy Microanalysis, Volume 9, 2003, pp. 296-310

[22] Hernandez P., Jimenez D., Kakadiaris I. A. et al., *Segmentation of neurons based on one-class classification*, IEEE 11th International Symposium on Biomedical Imaging (ISBI), 2014, pp. 1316-1319

[23] Hernandez E., Weiss G., *A first course on wavelets*, CRC Press,1996

[24] Hong Y. H., Khotanzad A., *Invariant image recognition by zernike moments*, IEEE Transactions on Pattern Analysis Machine Intelligence, Volume 12(5), 1990, pp. 489-497

[25] Hu M. K., *Visual pattern recognition by moment invariants*, IRE Transactions on Information Theory, Volume 8(2), 1962, pp. 179-182

[26] Huang Y., Zhou X., Miao B., Lipinski M. et al., *A computational framework for studying neuron morphology from in vitro high content neuron-based screening*, Journal on Neuroscience Methods, Volume 190, 2010, pp. 299-309

[27] Jimenez D., Labate D., Kakadiaris I. A., Papadakis M., *Improved automatic centerline tracing for dendritic and axonal structures*, Neuroinformatics 13(2), 2015, pp. 227-244

[28] Jimenez D., Papadakis E., Labate D., Kakadiaris I. A., *Improved automatic centerline tracing for dendritic structures*, 10th IEEE International Symposium on Biomedical Imaging (ISBI), 2013, pp. 1050-1053

[29] Jimenez D., Labate D., Papadakis M., *Directional analysis of 3d tubular structures via isotropic well-localized atoms*, Applied and Computational Harmonic Analysis, 2015, pp. 1-18

[30] Keeling S. L., Stollberger R., *Nonlinear anisotropic diffusion filtering for multiscale edge enhancement*, Inverse Problems, Volume 18(1), 2002

[31] Kutyniok G., Labate D., *Shearlets: Multiscale analysis for multivariate data*, Birkhauser, Boston, 2012

[32] Kutyniok G., Shahram M., Zuang X., *ShearLab: A rational design of a digital parabolic scaling algorithm*, SIAM Journal on Imaging Sciences, Volume 5(4), 2012, pp. 1291-1332

[33] Labate D., Laezza F., Negi P., Ozcan B., Papadakis M., *Efficient processing of fluorescence images using directional multiscale representations*, Mathematical Modelling of Natural Phenomena, Volume 9, Number 5, 2014, pp. 177-193

[34] Lang P., Yeow K., Nichols A., Scheer A., *Cellular imaging in drug discovery*, Nature Reviews Drug Discovery, Volume 5, 2006, pp. 343-356

[35] Lindeberg T., *Feature detection with automatic scale selection*, International Journal of Computer Vision, Volume 30(2), 1998

[36] , Lowe D. G., *Object recognition from local scale-invariant features*, Proceedings of International Conference on Computer Vision, Volume 2, 1999, pp. 1150-1157

[37] Mallat S., *A wavelet tour of signal processing.* Academic Press, San Diego, CA, 1998

[38] Negi P. N., Labate D., *3-D discrete shearlet transform and video processing*, IEEE Transactions on Image Processing, Volume 21, 2012, pp. 2944-2954

[39] Osher S., Fedkiw R., *Level set methods and dynamic implicit surfaces*, Applied Mathematical Sciences, New York, Springer, 2003

[40] Ozcan B., Labate D., Jimenez D., Papadakis M., *Directional and non-directional representations for the characterization of neuronal morphology*, Wavelets XV (San Diego, CA, 2013), SPIE Proceedings., Volume 8858, pp. 1050-1053

[41] Ozcan B., Negi P., Laezza F., Papadakis M., Labate D., *Automated detection of soma location and morphology in neuronal network cultures*, PLoS ONE 10(4): e0121886. doi: 10.1371/journal.pone.0121886

[42] Pawley J. B., *Handbook of biological confocal microscopy*, New York, Springer, 2006

[43] Perona M., Malik J., *Scale-space and edge detection using anisotropic diffusion*, Transactions on Pattern Analysis and Machine Intellegence, Volume 90(7), 1990, pp. 629-638

[44] Rodriguez A., Ehlenberger D. B., Hof P. R., Wearne S. L., *Rayburst sampling, an algorithm for automated three-dimensional shape analysis from laser scanning microscopy images*, Nature Protocols, Volume 1, 2006, pp. 2152-2161

[45] Mikolajczyk K., Schmid C., *Scale and affine invariant interest point detectors*, International Journal of Computer Vision, Volume 60(1), 2004, pp. 63-86

[46] Sethian J. A., *Level set methods and fast marching methods*, Cambridge University Press, 2 edition, 1999

[47] Shavkunov A. S., Wildburger N. C., Nenov M. N. et al., *The fibroblast growth factor 14voltage-gated sodium channel complex is a new target of glycogen synthase kinase 3 (GSK3)*, Journal of Biological Chemistry, Volume 288,2013, pp. 1937019385

[48] Sharma K., Choi S.Y., Zhang Y. et al., *High-throughput genetic screen for synaptogenic factors: identification of $\{LRP6\}$ as critical for excitatory synapse development*, Cell Reports, Volume 5, 2013, pp. 1330-1341

[49] Sumengen B., http://barissumengen.com/level_set_methods/index.html, Vision Research Lab at UC Santa Barbara, 2005

[50] Svoboda K., *The past, present, and future of single neuron reconstruction*, Neuroinformatics, Volume 9, 2011, pp. 87-98

[51] Teague M. R., *Image analysis via the general theory of moments*, Optical Society of America, Volume 70(8), 1979, pp. 920-930

[52] Vallotton P., Lagerstrom R., Sun C. et al., *Automated analysis of neurite branching in cultured cortical neurons using hca-vision*, Cytometry Part A, Volume 71, 2007, pp. 889-895

[53] Weickert J., *Anisotropic diffusion in image processing*, ECMI Series, Teubner-Verlag, Stuttgart, Germany, 1998

[54] Weaver C. M., Pinezich J. D. et al., *An algorithm for neurite outgrowth reconstruction,* Journal of Neuroscience Methods, Volume 124, 2003, pp. 197-205

[55] Yi S., Labate D., Easley G. R., Krim H., *A shearlet approach to edge analysis and detection*, IEEE Transactions on Image Processing, Volume 18, 2009, pp. 929-941

[56] You Y., Xu W., Tannenbaum A., Kaveh M., *Behavioral analysis of anisotropic diffusion in image processing*, IEEE Transactions on Image Processing, Volume 5(11), 1996, pp. 1539-1553

[57] You Y., Kaveh M., *Fourth order partial differential equations for noise removal*, IEEE Transactions on Image Processing, Volume 9(10), 2000, pp.1723-1730

[58] Yan C., Li A., Zhang B. et al., *Automated and accurate detection of soma location and surface morphology in large-scale 3d neuron images,* PLoS ONE 8(4), 2013, pp. 1-12